



Dynamic In Situ Nonlinear Inelastic Response of a Deep Medium Dense Sand Deposit

Amalesh Jana¹ and Armin W. Stuedlein, M.ASCE²

Abstract: This study presents the use of controlled blasting for the determination of the in situ dynamic response of a sand deposit at a depth of 25 m under effective overburden stresses of approximately 250 kPa. The experiments were performed to establish the suitability of blasting as a seismic energy source for the quantification and evaluation of dynamic constitutive soil properties, including the coupled degradation of shear modulus, G, and generation of excess pore pressure, u_e , with shear strain, γ . The ground motion characteristics associated with controlled blasting were quantified, indicating that compression waves operate at frequencies too high to generate significant particle displacements and corresponding strains. The shear waves generated due to near- and far-field unloading of the initial compression wave were found to control the soil response, and were associated with frequencies common in earthquake ground motions. The three blast experiments provide the basis for the in situ observation of constitutive soil properties, including the threshold shear strains to trigger soil nonlinearity and residual excess pore pressure, ue,r, as well as changes in constitutive responses as a result of alterations in the soil fabric and geostatic stress state. Field drainage during the experiments was found to exert a significant influence on large-strain G, and its effects distinguish the in situ response from those observed in dynamic, fully undrained or constant-volume laboratory experiments. The linear-elastic threshold shear strain, γ_{te} , of the natural sand deposit ranged from 0.001% to 0.002% and the threshold shear strain to initiate $u_{e,r}$, γ_{tp} , ranged from 0.008% to 0.01% for the intact natural deposit. Reduction in normalized G of approximately $0.70G_{\max}$ was necessary to trigger $u_{e,r}$ within the intact natural sand deposit. The generation of u_e in the reconsolidated sand deposit was greater than the intact deposit, with γ_{tp} reducing to 0.002%–0.003%. The significantly reduced geostatic stress state inferred from shear wave velocity and settlement measurements facilitated comparison of the shear strain-excess pore pressure relationship for vertical effective stresses ranging from 44 to 256 kPa, and confirmed that such relationships are highly pressure dependent. DOI: 10.1061/(ASCE)GT.1943-5606.0002523. © 2021 American Society of Civil Engineers.

Introduction

The seismic response of deep deposits of liquefiable soils has presented the geotechnical profession with significant challenges, including the assessment of site response (i.e., amplification) and its evolution during an earthquake as soils soften under cyclic shear, liquefaction triggering, and the consequences of liquefaction (e.g., postcyclic volumetric strains). Laboratory-based assessments of the cyclic response of intact soil specimens are limited by the cost and complexity of retrieving undisturbed samples, which may require freezing and coring of the target soil deposit (e.g., Esposito et al. 2014). Whereas laboratory testing of reconstituted specimens can reveal certain trends in such contributing factors as mineralogy (Derakhshandi et al. 2008; Park and Kim 2013), particle morphology (Ashmawy et al. 2003; Xiao et al. 2018), and grain size distributions (Koester et al. 1994; Hazirbaba and Rathje 2009), relationships such as cyclic stress ratio vs. number of cycles or shear modulus reduction curves are governed by the method of reconstitution (e.g., Mulilis et al. 1977) and reflect the boundary and drainage conditions, loading frequencies, and compliance

Note. This manuscript was submitted on August 24, 2020; approved on January 25, 2021; published online on April 15, 2021. Discussion period open until September 15, 2021; separate discussions must be submitted for individual papers. This paper is part of the *Journal of Geotechnical and Geoenvironmental Engineering*, © ASCE, ISSN 1090-0241.

associated with the specific laboratory apparatus used to derive such relationships. These observations led Seed et al. (1983), for example, to conclude that field-based correlations to liquefaction triggering, through in situ penetration tests, and later shear wave velocity, may represent a more practical approach for assessing liquefaction triggering.

Evaluation of the dynamic in situ response of liquefiable soils serves to mitigate the obstacles noted above that are associated with laboratory-based characterization. For example, mobile shakers have been used to directly observe shear modulus degradation and generation of excess pore pressure with shear strain (Rathje et al. 2001, 2005; Cox et al. 2009; Chang et al. 2007; Stokoe et al. 2005, 2014; Roberts et al. 2016, 2017; Zhang et al. 2019). Careful collection, screening, and evaluation of liquefaction triggering case histories following field reconnaissance efforts has led to continuing refinements to simplified triggering procedures (e.g., Youd et al. 2001; Moss et al. 2006; Kayen et al. 2013; Boulanger and Idriss 2016). However, these field-based examples are often representative of shallow depths-for example, 3-4 m (with mobile shaking; van Ballegooy et al. 2015) or 12 m (triggering case histories; Boulanger and Idriss 2016), with uncertain estimates of the loading often prevailing in the latter case. In the field, excess pore pressure generation is more rapid than in conventional undrained or constant-volume laboratory element tests due to the 2D and/or 3D nature of earthquake ground motions and redistribution of excess pore pressure during shaking, which is difficult to simulate in the laboratory (Dobry and Abdoun 2015). Improvements in the understanding of the system response of liquefiable soil profiles (e.g., Cubrinovski et al. 2019) and instrumented arrays (e.g., Zeghal and Elgamal 1994) and their interpretations (e.g., Kramer and Greenfield 2019) serve to further clarify the deep in situ dynamic response of liquefiable soils. Specific key questions

¹Graduate Research Assistant, School of Civil and Construction Engineering, Oregon State Univ., 101 Kearney Hall, Corvallis, OR 97331. ORCID: https://orcid.org/0000-0003-1130-4037

²Professor, School of Civil and Construction Engineering, Oregon State Univ., 101 Kearney Hall, Corvallis, OR 97331 (corresponding author). ORCID: https://orcid.org/0000-0002-6265-9906. Email: armin.stuedlein@oregonstate.edu

have been identified with regard to the response of deep liquefiable deposits: (1) Is the threshold shear strain to trigger excess pore pressure, γ_{tp} , and continued generation of excess pore pressure dependent on confining pressure? (2) Can the theoretically robust cyclic strain approach (e.g., Dobry et al. 1981, 1982) be demonstrated under realistic, deep in situ conditions? and (3) What is the role of drainage on cyclic softening during shaking, critical for long-duration subduction zone earthquakes?

This paper discusses the application of controlled blasting to seismically excite an instrumented array installed at 25-m depth and characterize the in situ dynamic response of a medium dense sand deposit at the Port of Portland in Oregon. First, the subsurface conditions and experimental program are presented. Select results from a laboratory test program are presented, including cyclic direct simple shear (DSS) tests on reconstituted specimens. The blast-induced ground motions are then characterized in terms of component body waves and their strain potential, frequency content, and dimensionality. Then, relationships between the in situ shear strain and excess pore pressure and shear modulus degradation are presented, and are compared and contrasted with similar relationships derived for reconstituted sands and large-scale and centrifuge experiments. This unique dataset provides a context for discussion of the aforementioned questions identified for the dynamic response of deep liquefiable soil deposits.

Experimental Setting and Soil Characterization

Site and Subsurface Conditions

The experiments described herein were conducted at a site on the Port of Portland property situated in proximity to the Columbia River within the Portland basin. Subsurface investigations related to the deposit of interest included cone penetration tests (CPTs), standard penetration tests (SPTs) with split-spoon sampling, and geophysical tests. Explorations (Fig. 1) and pore pressure transducers (PPTs) revealed typical fluctuations in the depth to the groundwater table that range from 3.0 to 7.3 m, and which correspond to seasonal changes in the Columbia River stage and transient dewatering operations performed on port properties. Overburden stress corrections to penetration resistances and effective stresses during the experiments were computed using the observed piezometric conditions at the time of the exploration or observation. The stratigraphy at the site consists of dredge sand and silty sand hydraulic fill ranging from 5 to 6 m in depth, underlain by a ~2-m thick layer of young, alluvial, loose clean sand (Section A-A'; Fig. 2). This layer is underlain by a 4- to 6-m thick alluvial, medium stiff, clayey

silt (ML and MH) overbank deposit, described by Jana and Stuedlein (2020) and Jana et al. (2021), followed by the deep deposit of medium dense, fine, clean sand (SP) and sand with silt (SP-SM) that forms the basis for the current study. Grain size analyses indicated that fines contents, FC, of the deep deposit of medium dense sand generally ranged from 3% to 12%, with median grain size, D_{50} , and coefficient of uniformity, C_u , ranging from 0.21 to 0.28 mm and 1.8 to 5.1, respectively [Fig. 3(a)]. Scanning electron microscopy (SEM) images of sand retrieved from split-spoon samples indicate that the sand particles are angular to subangular in shape, are occasionally mantled by fine, platy silt and clay particles, and appear cemented in some images. The shallower silt and deeper sand layers were deposited in the late Pleistocene era (Evarts et al. 2016); however, no evidence for significant aging was identified using the measured-to-estimated velocity ratio (Andrus et al. 2009) or small-strain stiffness-to-penetration resistance ratio (Schneider and Moss 2011). Split-spoon samples subjected to gasometric determination of calcium carbonate content (ASTM 2014) revealed very low concentrations of <0.1% (M. G. Gomez, personal communication, 2019). Within the 2.4-m window of the instrumented array (described below) over depths of 23.8-26.2 m, the sand is characterized by an average corrected cone tip resistance, q_t , of 11.8 MPa; overburden stress, clean sand-corrected cone tip resistance, q_{c1Ncs} , of 137 (derived following Boulanger and Idriss 2014); overburden stress, energy- and clean sand-corrected SPT blow count of 15 blows per foot (bpf) (derived following Boulanger and Idriss 2016 with energy measurements); and average relative densities, D_r , of 40% (derived via SPT; Cubrinovski and Ishihara 1999) and 47% (derived via CPT; Mayne 2007). A representative soil behavior type index (Robertson 2009), I_c , for the sand within the instrumented array is approximately 1.9 (Fig. 2).

Laboratory Characterization of Reconstituted Sand Specimens

Sand specimens reconstituted from split-spoon samples of the Sand Array were used to provide a minimum basis for the interpretation of, and comparison to, the observed in situ dynamic responses. Although many methods for reconstituting specimens exist, each with their advantages and disadvantages (Mulilis et al. 1977; Park and Silver 1975; Ladd 1977; Seed 1979), trial laboratory efforts determined that air-pluviation producing similar D_r as correlated to penetration resistance and described above could yield a similar shear wave velocity, V_s , as that observed in situ. The V_s of the reconstituted DSS test specimens with vertical effective consolidation stress, σ'_{vc} , was measured using bender elements and is

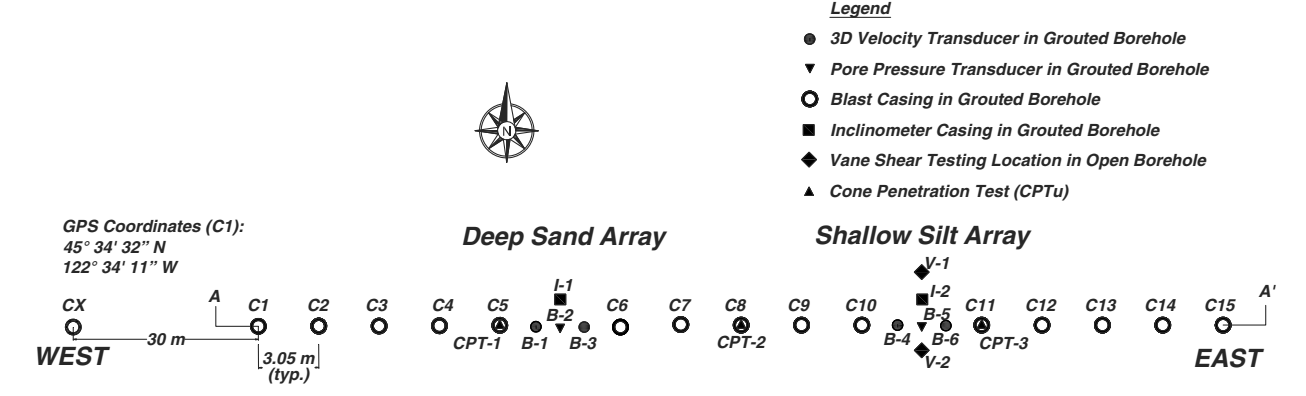


Fig. 1. Site and exploration plan indicating blast casings and instruments comprising the Sand and Silt Arrays. Note: Borehole GRI-17-B-1 (Fig. 2) located approximately 35 m north of C8.

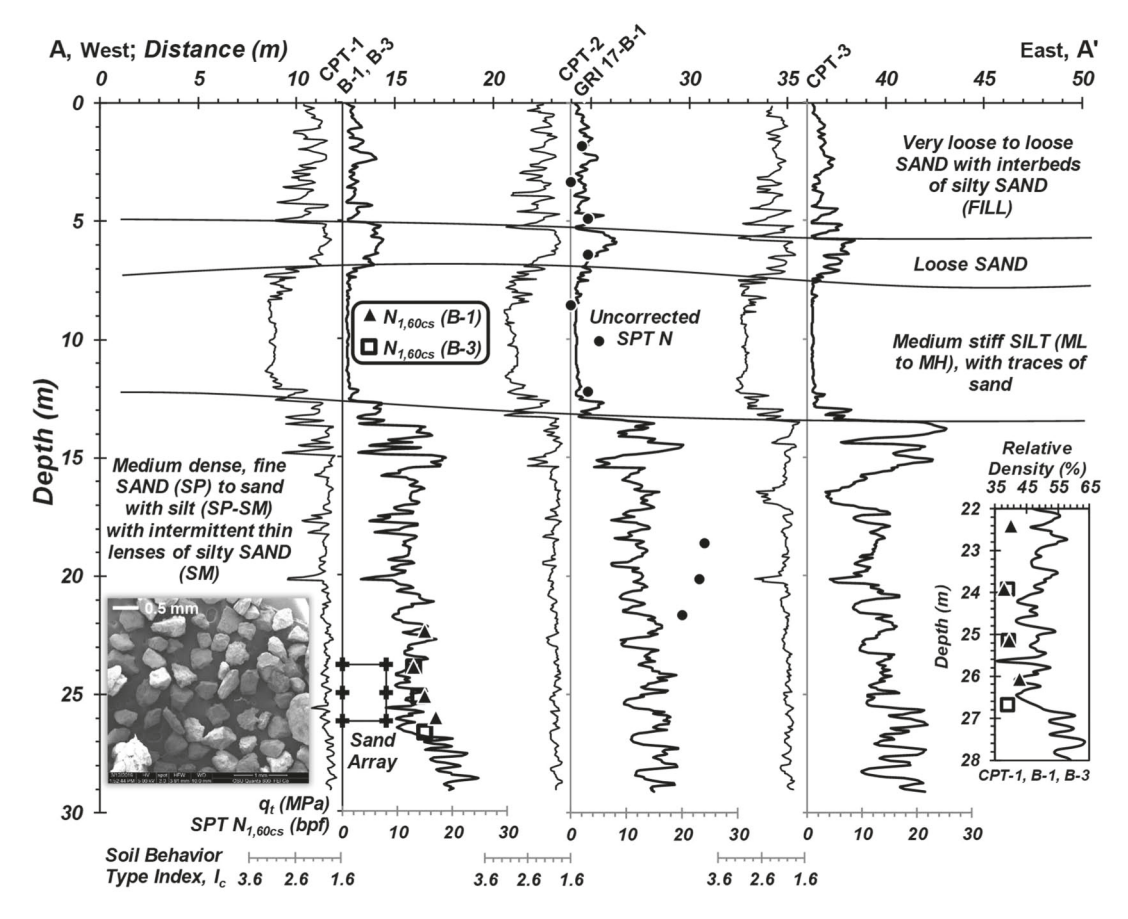


Fig. 2. Subsurface cross section A-A' (Fig. 1) indicating $\bar{q}_t = 11.8$ MPa ($\bar{q}_{c1Ncs} = 137$), $\bar{N}_{1,60cs} = 15$ bpf, and CPT-based $\bar{D}_r = 47\%$ and SPT-based $\bar{D}_r = 40\%$ (right inset) within the Sand Array; and scanning electron micrograph of sand particles retrieved from the Sand Array (left inset).

shown in the Fig. 3(b) inset. The average V_s of the specimens at the in situ $\sigma'_{v0} = \sigma'_{vc} = 240$ kPa and $D_r = 51\%$ was 218 m/s, similar to that measured in situ, as described below. Monotonic constant-volume DSS tests on specimens reconstituted from split-spoon samples with $D_r = 45\%$ indicated an initially contractive response to shear, with phase transformation and critical state friction angles of approximately 29° and 32°, respectively, at the average in situ $\sigma'_{v0} = 240$ kPa.

Strain-controlled constant-volume cyclic DSS tests were conducted on dry sand specimens reconstituted in the same manner and similar D_r . Uniform sinusoids of varying shear strain amplitude characterized with a loading frequency 0.1 Hz were applied to individual specimens. Fig. 3(b) shows the variation of residual excess pore pressure ratio, $r_{u,r}$, defined as the ratio of residual excess pore pressure, $u_{e,r}$, at the end of each loading cycle and σ'_{vc} , with shear strain for the number of loading cycles, N, ranging from 5 to 30. The definition of $r_{u,r}$ implemented herein differs somewhat from that of Dobry et al. (1982), which was based on the excess pore pressure, u_e , measured at intermediate or terminal stoppages of cyclic testing (perhaps to ensure equilibration of the excess pore pressure field in the cyclic triaxial test specimen). The use of dry specimens and $\Delta \sigma'_v$ as the basis for u_e (Dyvik et al. 1987) forms the basis for the definition of $r_{u,r}$ used herein. The lower inset within Fig. 3(b) demonstrates the convergence of near-zero $r_{u,r}$ at $\gamma_{DSS} = 0.008\%$, identifying the cyclic threshold shear strain, $\gamma_{tp}=0.008\%$. Increases in shear strain amplitude produce corresponding increases in $r_{u,r}$ to result in residual liquefaction (i.e., $r_{u,r} = 100\%$) at $\gamma_{DSS} \approx 1\%$ for N = 30. These laboratory-based observations are compared with in situ observations described below.

Experimental Program

Instrumentation Comprising the Sand Array

Fig. 4 presents the geometry of the Sand Array placed to capture blast-induced ground motions and designed following the general protocols developed by Cox et al. (2009). The Sand Array, including triaxial geophone packages (TGPs) and PPTs, facilitates the evaluation of time-varying shear modulus, G, and excess pore pressure evolution with shear strain amplitude following the finite element methodology proposed by Rathje et al. (2001, 2005), Chang et al. (2007), Cox et al. (2009) and implemented by Stokoe et al. (2014), Sahadewa et al. (2015), and Roberts et al. (2016, 2017). The TGPs consisted of three 28-Hz geophones, a triaxial MEMS accelerometer, and an inertial motion unit. The TGPs were suspended from the inclinometer casing placed within 200-mm diameter boreholes, B-1 and B-3, excavated using mud-rotary methods and grouted in place using a cement-bentonite grout with proportions selected to simulate the stiffness of sand layer following Mikkelsen and Green (2003). The TGPs form two nominally rectangular finite elements, with the TGPs serving as the nodes and where measured particle velocities could be integrated. The inclinometers enabled determination of the distance between TGPs that is necessary to compute body wave velocities in view of meandering borehole trajectories, as described by Jana et al. (2021). Likewise, PPTs were placed and grouted within mud-rotary borehole B-2 (Figs. 1 and 4). A separate inclinometer casing, I-1 (Fig. 1), placed within a flexible corrugated plastic sheathing fitted with sondex settlement rings, was installed using mud-rotary drilling techniques to a depth of 28.3 m, approximately 1.2-m north of

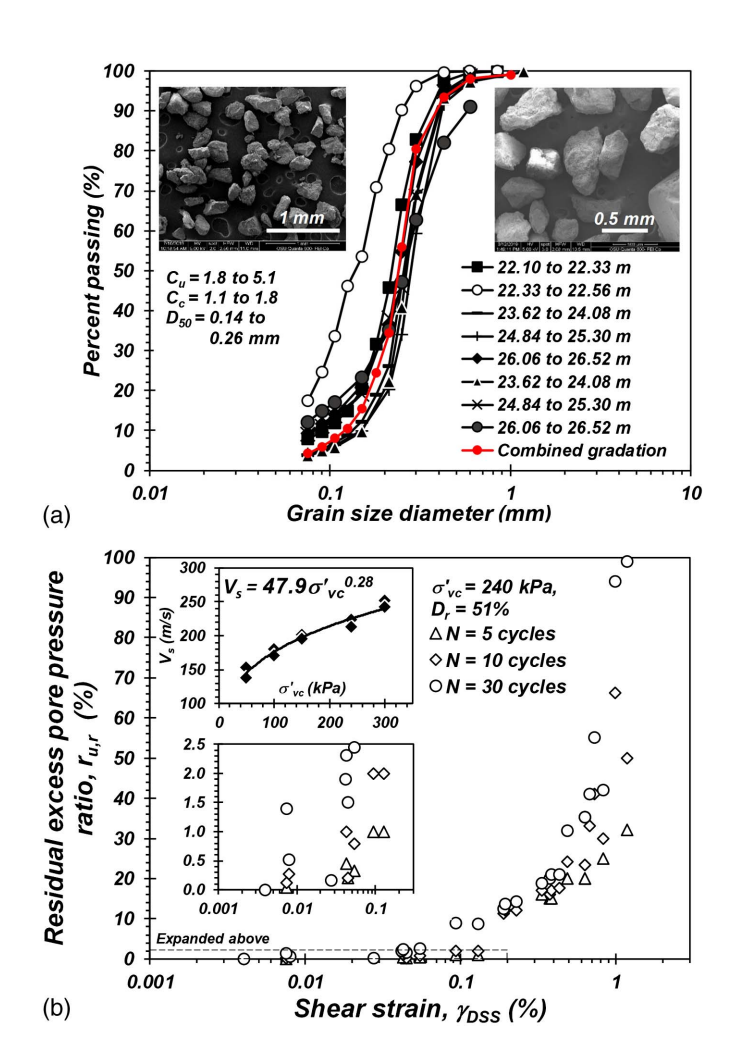


Fig. 3. Laboratory characterization of the sand retrieved from the Sand Array: (a) grain size distributions with inset SEM images of sand particles; and (b) variation of residual excess pore pressure with shear strain derived from strain-controlled constant-volume cyclic DSS tests on reconstituted specimens with $D_r = 51\%$, and sheared using a loading frequency of 0.1 Hz, with inset presenting the variation of V_s with σ'_{nc} .

the planar Sand Array. Significant effort was necessary to satisfactorily calibrate instruments and determine the as-built tilt and orientation of, and distance between, individual sensors; the reader is referred to Jana et al. (2021) for details regarding the execution of such an instrumentation program. Following installation, downhole geophysical tests were conducted to determine baseline compressive wave velocities, V_p , and V_s as described below.

Blast Programs Executed

Three separate blast events comprise the experimental program undertaken to capture the fundamental dynamic soil response within the Sand Array: (1) Test Blast Program (TBP), conducted on October 3, 2018; (2) Deep Blast Program (DBP), conducted on October 4, 2018; and (3) Shallow Blast Program (SBP), conducted on October 5, 2018. The TBP was performed to evaluate site-specific attenuation of ground motions, assess the operability of instruments and data acquisition, and to establish linear-elastic, small-strain crosshole V_s in the sand and silt layers. The primary objective of the DBP was to dynamically excite the soils within the Sand Array, whereas the main objective of the SBP was to excite

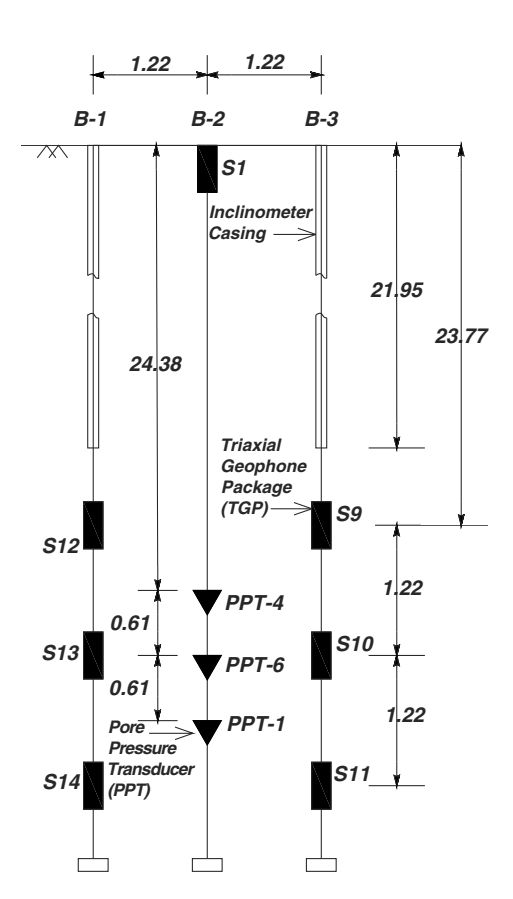


Fig. 4. Instruments comprising the Sand Array (all units in meters). Note: Inclinometer I-1 not shown for clarity.

the soils within the Silt Array (Fig. 1; not described herein). Data were acquired in each array and blast program to evaluate the consequences of each dynamic event on possible changes in constitutive response.

The explosives and detonation system consisted of Pentex cast boosters with i-kon electronic detonators and Cordtex detonation cord (Orica, Victoria, Australia). The detonation velocity and pressure associated with the Pentex cast boosters were 7,900 m/s and 24 MPa, respectively. During the eight-charge TBP, all charges were placed within blast casing CX, located 30-m west of the west-ernmost blast casing comprising the linear, east-west alignment (i.e., casing C1, Fig. 1). The DBP consisted of 30 charges distributed within blast casings C1 through C10, with small charges (i.e., 90-g TNT-equivalent) placed at the farthest locations from the Sand Array to produce elastic soil responses. Table 1 summarizes the detonation and charge time-histories for the three blast programs, indicating detonation sequence, the depth, and casing for

Table 1. Charge weight, depths, and schedule of detonation comprising the three blast programs

Blast program	Detonation sequence and charge location	Time (s)	Depth (m)	Charge weight (g)	
Test Blast	1-CX	0	6.6	227	
Program	2-CX	1	8.2	454	
_	3-CX	2	10.2	907	
	4-CX	3	12.6	1,814	
	5-CX	4	18.2	454	
	6-CX	5	20.2	907	
	7-CX	6	22.6	1,814	
	8-CX	7	25.7	3,628	

Table 1. (Continued.)

Blast program	Detonation sequence and charge location	Time (s)	Depth (m)	Charge weight (g)
Deep Blast	1-C1	0	23.14	90
Program	2-C10	1	13.69	90
	3-C1	2	25.27	90
	4-C10	3	23.44	90
	5-C1	4	26.84	150
	6-C10	5	26.56	150
	7-C2	6	22.79	228
	8-C9	7	22.64	228
	9-C2	8	24.70	456
	10-C9	9	24.22	456
	11-C2	10	26.59	912
	12-C9	11	26.59	912
	13-C3	12	19.91	1,824
	14-C8	13	19.91	1,824
	15-C3	14	22.66	1,824
	16-C8	15	22.96	1,824
	17-C3	16	25.87	3,648
	18-C8	17	25.87	3,648
	19-C4	18	19.10	3,648
	20-C7	19	19.10	3,648
	21-C4	20	22.39	2,721
	22-C7	21	22.70	2,721
	23-C4	22	26.04	2,721
	24-C7	23 24	25.74	2,721
	25-C5 26-C6	25	23.39 21.25	1,361
	27-C5	26	24.15	1,361 1,361
	28-C6	27	24.13	1,361
	29-C5	28	26.53	912
	30-C6	29	26.53	912
Shallow Blast	1-C6	0	8.21	90
Program	2-C15	1	7.29	90
	3-C6	2	9.73	90
	4-C15	3	9.73	90
	5-C6	4	11.97	150
	6-C15	5	11.59	150
	7-C7	6	7.56	228
	8-C14	7	7.56	228
	9-C7	8	9.28	456
	10-C14	9	9.89	456
	11-C7	10	11.29	912
	12-C14	11	11.77	912
	13-C8	12	5.82	1,824
	14-C13	13	6.20	1,824
	15-C8	14	8.65	912
	16-C13	15	9.16	912
	17-C8	16	11.29	912
	18-C13	17	11.39	912
	19-C9	18	4.10	456
	20-C12	19	4.10	456
	21-C9	20	7.76	456 456
	22-C12	21	7.76	456
	23-C9	22	11.52	228
	24-C12	23	11.88	228
	25-C10	24	6.66	150
	26-C11	25	6.66	150
	27-C10	26	9.40	150
	28-C11 29-C10	27 28	9.40 11.54	150 150
			1 1 3/4	

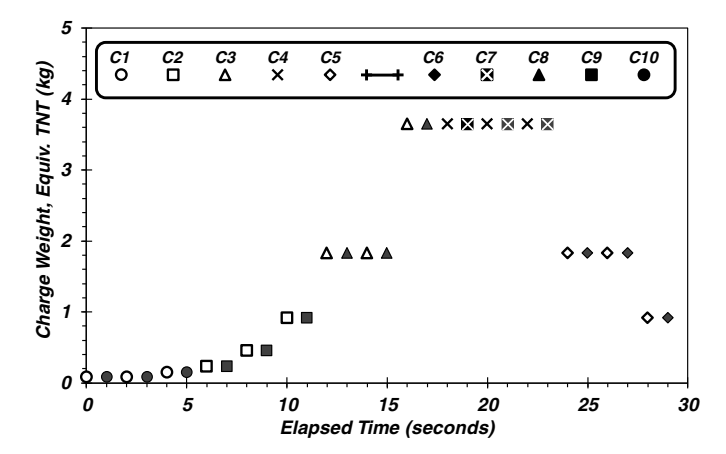


Fig. 5. Charge detonation time-history implemented in the Deep Blast Program, indicating their spatial distributions relative to the Sand Array and the use of small charges at the farthest distances to produce elastic soil responses (compare to Fig. 1).

each charge. Fig. 5 presents the charge detonation and location time-history implemented, indicating a progressive increase in charge weight and decrease in distance to the Sand Array, where charges were detonated sequentially on either side of the Sand Array to reverse the polarity of peak shear strain amplitudes. Owing to the geometry of the planar Sand Array and linearly aligned blast casings, the body waves generated could be assumed to represent 2D motions for many of the blasts, as described below.

Computation of Shear Strain

The experiment and instrumented Sand Array (Figs. 1 and 4) were designed to facilitate calculation of shear strain following the approach proposed by Cox et al. (2009). This methodology has been implemented to deduce dynamically imposed shear strain in a variety of soils (Rathje et al. 2001, 2005; Cox et al. 2009; Chang et al. 2007; Stokoe et al. 2014; Sahadewa et al. 2015; Roberts et al. 2016, 2017; Cappa et al. 2017; Zhang et al. 2019). Accordingly, the Sand Arrays were designed to formulate two 2D isoparametric finite elements (Fig. 4). In this formulation, the east-west or longitudinal, x, and vertical, z, particle displacements, D_x and D_z , of the four nodes of each element are calculated from the measured particle velocities, V_x and V_z , which are used along with appropriate shape functions to deduce the 2D Cauchy strain tensor (i.e., normal strains, ε_{xx} , ε_{zz} , and shear strain, γ_{xz}). Estimation of shear strain using the displacement method does not require the assumption of plane wave propagation, and can be used for any wave field, as demonstrated by Cox (2006). The two elements evaluated herein are constructed using TGP S10, S11, S14, and S13 (Element 1) and TGP S9, S10, S13, and S12 (Element 2; Fig. 4). The shear strain is computed from the full waveform of the particle motion including the compression or P-wave, the near-field shear or S-wave, and the far-field S-wave. The octahedral shear strain, γ_{oct} , computed from the Cauchy strain tensor for each element, corresponds to the location of the relevant PPT, the approximate midpoint of each element. The deviatoric strain invariant γ_{oct} may be computed from the Cauchy strain tensor for plane strain conditions (Cappa et al. 2017) as follows:

$$\gamma_{oct} = \left(\frac{2}{3}\right) \sqrt{(\varepsilon_{xx})^2 + (-\varepsilon_{zz})^2 + (\varepsilon_{zz} - \varepsilon_{xx})^2 + 6\left(\frac{\gamma_{xz}}{2}\right)^2} \quad (1)$$

where all variables have been previously defined.

Characterization of Blast-Induced Ground Motions

Controlled blasting has gained acceptance in geotechnical experimentation because of its ability to simulate excess pore pressure fields in situ with corresponding consequences (e.g., dissipationinduced settlement). Examples of previous experiments include the evaluation of stone columns, aggregate piers, timber piles, and earthquake drains to reduce seismically induced excess pore pressures (Ashford et al. 2000a, b; Rollins et al. 2004; Gianella and Stuedlein 2017; Amaroso et al. 2020), liquefaction-induced dragloads (Rollins and Strand 2006; Eshimwe et al. 2018; Kevan et al. 2019), lateral load transfer in liquefied soils (Ashford et al. 2004; Rollins et al. 2005, 2006; Weaver et al. 2005), and to deduce possible relationships between shear strain and excess pore pressure (Gohl et al. 2001). Whereas earthquake-induced ground motions are commonly assumed to produce vertically propagating, horizontally polarized shear waves (Seed 1979), blast-induced ground motions depend significantly upon the specific sourceto-site ray path and distance (Heelan 1953; Blair 2007, 2010; Vanbrabant et al. 2002, Gao et al. 2019). Detonation of buried explosives generates a radially propagating P-wave dominant wave front (Dowding and Hryciw 1986), producing an initial compressive stress followed by tensile hoop stresses (Narin van Court and Mitchell 1994). Upon unloading, shear stresses (i.e., S-waves) develop due to the expanding wave front and soil fabric anisotropy (Hryciw 1986; Fragaszy and Voss 1986). Although the peak amplitude of near-field P-wave acceleration and corresponding frequency content of blast-induced ground motions are significantly higher than earthquake ground motions, it is shown herein that the strain potential of the P-wave component of the motion is low and does not control the soil response, particularly for great ray path distances, due to its frequency content. Further, the velocity and displacement amplitudes associated with blast-induced ground motions are similar to those of earthquake motions (Gohl et al. 2001). The excess pore pressure response to the blast-induced ground motion within saturated soils results from changes in the total mean stress, and unloading-type shear strains producing transient mean effective stresses, p', which act on the soil skeleton. Critically, it is the unloading of the wave front and corresponding shear strains that are responsible for residual excess pore pressures (Gohl et al. 2001), despite their correlation to compressive strain amplitude (e.g., Charlie 1988, 1992, 2013). The experiments providing the basis for this work leverage great source-to-site distances and 2D geometry to improve the resolution of body wave components and their consequences observed at the Sand Array.

Dynamic Soil Response to P- and S-Waves

Dynamic loading arising from the detonation of explosive charges is complex and depends on the proximity of the soil of interest to the charge, charge weight, and charge geometry. For the experiments conducted herein, the loading is characterized by: (1) a compressive shockwave (i.e., the *P*-wave); (2) unloading of the shockwave that is directly followed by near-field shearing (i.e., an *S*-wave) generated due to the expanding shockwave geometry and soil anisotropy; and (3) shearing from a far-field *S*-wave generated at the location of the charge. Ishihara (1968) linked Biot's (1956a, b) finding that two kinds of *P*-waves exist depending on the frequency of loading relative to a characteristic frequency and the compressibility of soil components (i.e., soil grains, water, soil skeleton, and pore volume): (1) those in which there is no motion of the water and soil skeleton relative to one another and, thus, little attenuation of wave energy (i.e., a wave of the first kind); and

(2) those in which there is sufficient attenuation such that the wave energy propagates similar to diffusion processes (i.e., a wave of the second kind, a consolidation process). The wave of the first kind, which applies herein, can be further categorized based on its frequency and wavelength—a short wavelength with high frequency does not provide opportunity for movement of porewater during the period of loading, and therefore passes in a drained state. This differs from the scenario investigated by Fragaszy and Voss (1986), who conducted quasi-static undrained compression tests with large changes in total stress (e.g., 35 MPa) to evaluate the potential for compression-induced liquefaction upon unloading. The compression and release of solid grains and water subjected to the drained P-wave is coupled, and these components respond elastically without grain fracture (Perry et al. 2015) for the P-wave-induced excess pore pressures generated in the current experiments (~5 MPa or less), such that there is no compression-induced slippage between the grains, no change to soil fabric, and no residual excess pore pressure. Unloading of the passing P-wave, however, triggers the generation of the low-frequency near-field S-wave, which may pass in an undrained state due to its predominant frequency (Ishihara 1968) and induce slippage between the grains and, therefore, changes to the soil fabric and residual excess pore pressure can result depending on the amplitude of the resulting shear strain (Martin et al. 1975; Dobry et al. 1982).

Fig. 6 places the foregoing discussion into the context of the DBP; characteristic particle velocities, V_x and V_z , measured using TGP S13 and the corresponding displacements, D_x and D_z , normalized by their respective maximums, are shown in Figs. 6(a and b) and Figs. 6(d and e) for a large distance, small charge weight and small distance, and large charge weight scenario, respectively. The P-wave is immediately followed by local shearing along the longitudinal direction, x, of particle motion due to the near-field SV-wave generated from the 3D seismic disturbance (Sanchez-Salinero et al. 1986) as shown in Figs. 6(a and d) for the two different scenarios. The initial, dominant local shear wave is designated as SV_x , which is accompanied to a lesser degree (i.e., in terms of velocity) by an SV-wave with particle motion transverse to the direction of wave travel, termed SV_z , and shown in Figs. 6(b and e). For the small charge weight-large distance scenario [Figs. 6(a and b)], the far-field SV-wave (with the transverse SV_z -wave dominant) arrives approximately 0.065 s after the P-wave. The P- and SVwaves are clearly identified by the differences in their frequency content, f, the former of which is two orders of magnitude greater than the latter, regardless of near- or far-field conditions. As blasting continues with increasing charge weight and decreasing distance (Fig. 5), $u_{e,r}$ rises and V_s and G degrade, such that local and far-field SV-waves become superimposed upon one another (Sanchez-Salinero et al. 1986), as shown in Figs. 6(d and e).

That the maximum particle velocities of the SV_x - and SV_z -wave are 50%–75% of the maximum P-wave velocities is of little consequence, owing to the differences in frequency content, as demonstrated by the corresponding particle displacements. For a small charge weight and large distance, the loading portion of the P-wave is responsible for 50% of $D_{\rm max}$ [Fig. 6(a)], whereas for large charge weights and small distances, the loading portion of the P-wave is responsible for just 5%-10% of D_{max} [Fig. 6(d)]. The excess pore pressure responses [Figs. 6(c and f)] indicate a clear correlation in frequency content for the body wave components comprising the blast-induced ground motions. Fig. 6(c) demonstrates the soil response in the nonlinear-elastic regime, with a maximum incremental octahedral shear strain, $\Delta \gamma_{oct,max}$, of 0.0066% that occurs during passage of the far-field SV_z-wave, and the development of zero $u_{e,r}$, despite a maximum P-wave-induced excess pore pressure ratio, $r_{u,p\text{max}}$, of 90.2%. The P-wave passes in a drained manner

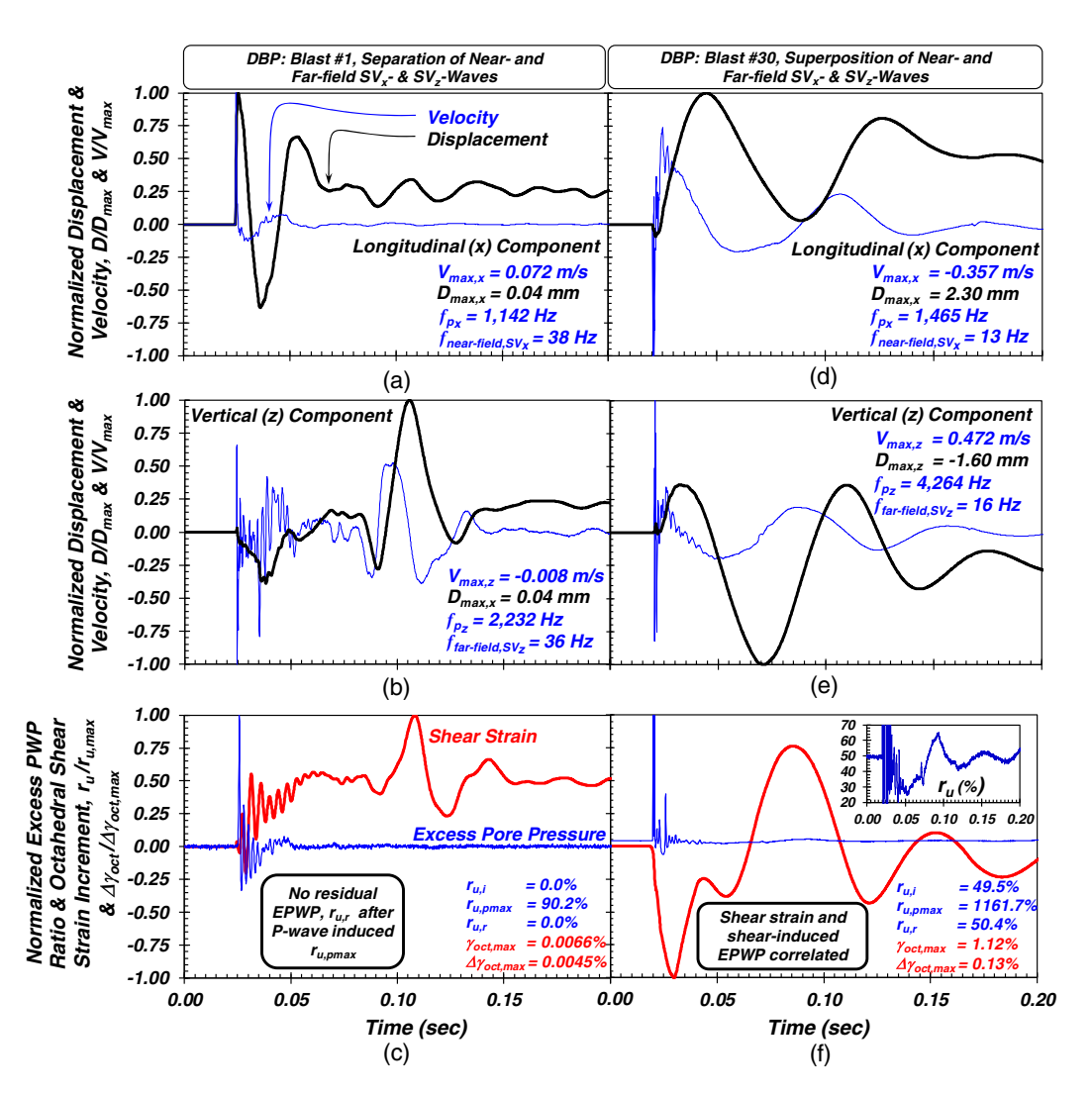


Fig. 6. Normalized velocity and displacement for (a) the longitudinal and (b) the vertical component in response to a 90-g charge detonated 14 m from TGP S13; and (c) corresponding normalized excess pore pressure ratio and octahedral shear strain increment in Element 1. Normalized velocity and displacement for (d) the longitudinal and (e) the vertical component in response to a 912-g charge detonated 4.6 m from TGP S13; and (f) corresponding normalized excess pore pressure ratio and octahedral shear strain increment in Element 1. Note: f = predominant frequency for a given body wave component; EPWP = excess porewater pressure; $r_{u,pmax}$ = maximum P-wave-induced excess pore pressure ratio; $r_{u,i}$ = initial excess pore pressure (prior to a given blast); and $r_{u,r}$ = residual excess pore pressure.

(Ishihara 1968) and the SV_z -wave is of sufficiently low amplitude to prevent grain slippage and generation of $u_{e,r}$ (Martin et al. 1975; Dobry et al. 1982). No shear strain occurs until the ephemeral P-wave unloads and the local SV-wave is generated. The case in Fig. 6(f) further demonstrates the effect of superimposed nearand far-field SV-waves that are responsible for shear strain and its correlation to displacement and excess pore pressure ratio, r_u , time-histories. These observations may serve to dispel criticisms that blast-induced ground motions are dominated by P-waves and that findings from such experiments may not be immediately transferrable to earthquake engineering applications. In fact, the frequency content of the P-wave is so large as to prevent significant displacement for the source-to-site distances evaluated, and is not responsible for the generation of $u_{e,r}$ [Fig. 6(c)]. SV-waves, whether derived from local shearing associated with near-field effects or from the far field, are responsible for the maximum induced displacements, the corresponding shear strain, and generation of residual excess pore pressure as suggested by Gohl et al. (2001).

Figs. 7(a-c) present the full particle velocity time-histories recorded in TGP S13 during the Test, Deep, and Shallow Blast Programs. Because the charges for the TBP and SBP were detonated relatively far from the Sand Array or did not provide significant energy outside the predominant envelope of the radiation field (Heelan 1953), particle velocities were significantly lower for these programs compared with those of the Deep Blast Program. However, the particle velocities (or, more appropriately, particle displacements) associated with the SBP were sufficient to induce a significant inelastic soil response due to the changes in the stress field within the sand resulting from volumetric strains following the DBP and corresponding soil arching over the Sand Array, as described below. The large range in peak velocity amplitudes (0.0006-2.08 m/s) suggest that future controlled blasting programs can achieve characteristic peak velocities associated with specific earthquake magnitudes and distances-for example, the range of 0.003–0.8 m/s for M_w ranging from 5.0 to 8.0 and 1 to 199 km, suggested by the ground motion model proposed by Campbell and Borzognia (2008).

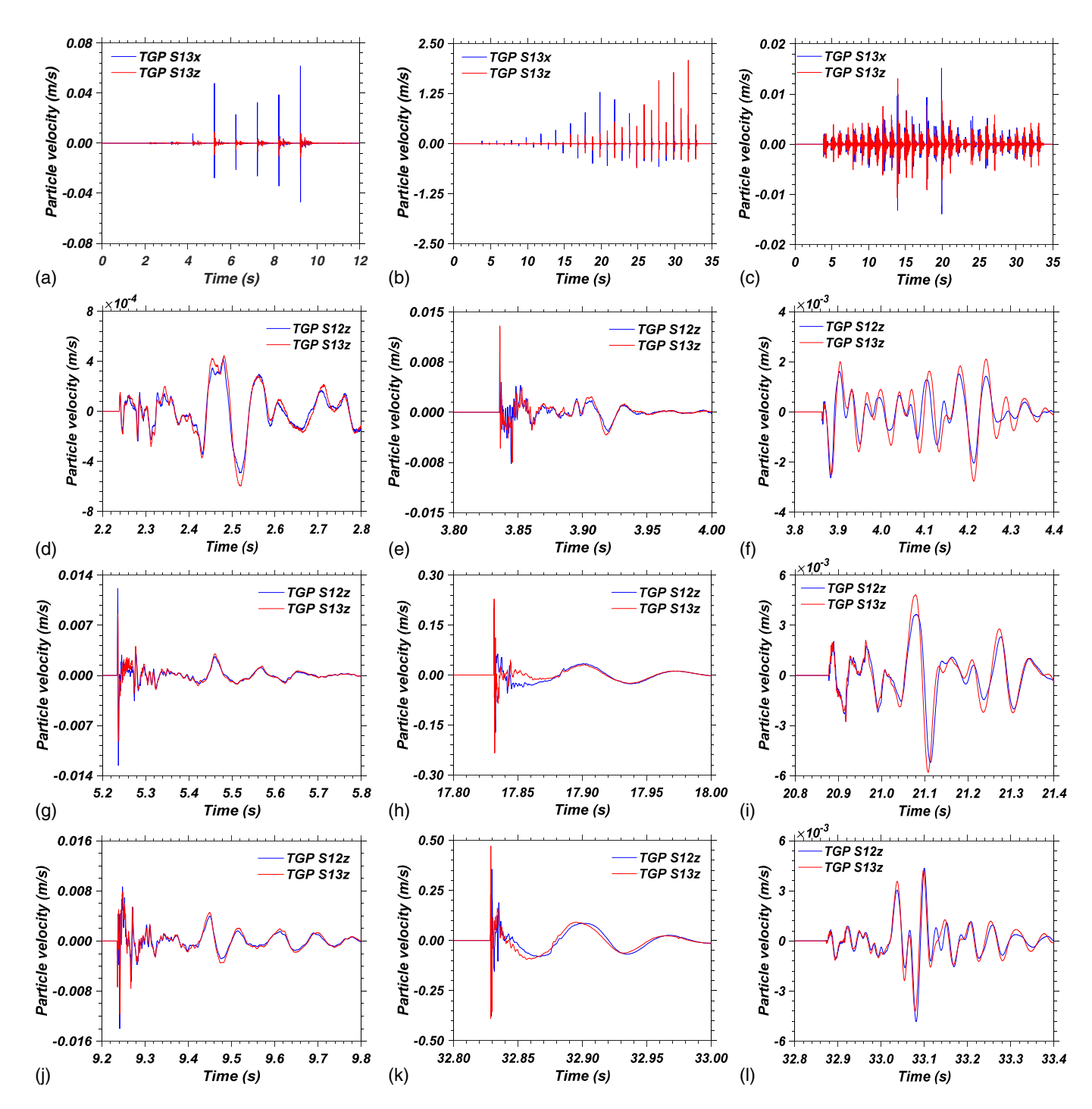


Fig. 7. Examples of particle velocity time-histories recorded in TGP 13 during (a) Test Blast Program (TBP); (b) Deep Blast Program (DBP); and (c) Shallow Blast Program (SBP); and comparison of the body wave amplitudes and phases of two vertically separated geophones located within the same borehole: (d) TBP Blast #1; (e) DBP Blast #1; (f) SBP Blast #1; (g) TBP Blast #4; (h) DBP Blast #15; (i) SBP Blast #18; (j) TBP Blast #8; (k) DBP Blast #30; and (l) SBP Blast #30.

Frequency Content of Ground Motions

The typical predominant frequencies of the body wave components measured during the DBP are presented in Fig. 8 for TGPs S11 and S13. Initially, the range in predominant f for the P-waves spanned \sim 300 to 2,000 Hz and increased as the distance to the Sand Array decreased, eventually ranging from 1,300 to 4,800 Hz. The increase in f with the decrease in ray path distance resulted from the decreased attenuation and corresponding filtering of the higher frequencies. The frequency content of the SV-waves did not depend

on the location of their generation (i.e., local near field or far field); f generally ranged from ~25 to 60 Hz early in the DBP and decreased with decreasing ray path distance, increasing $u_{e,r}$, and increasing γ , ultimately declining to as low as 7.7 Hz as the sand progressively softened under dynamic shear. Between the 20th and 25th charge, the decreasing trend in f reversed as drainage initiated (described below). These SV-wave frequencies correspond to those observed within earthquake ground motions and, due to their low magnitude, the SV-waves supplied the largest strain energy of the blast-induced body wave components.

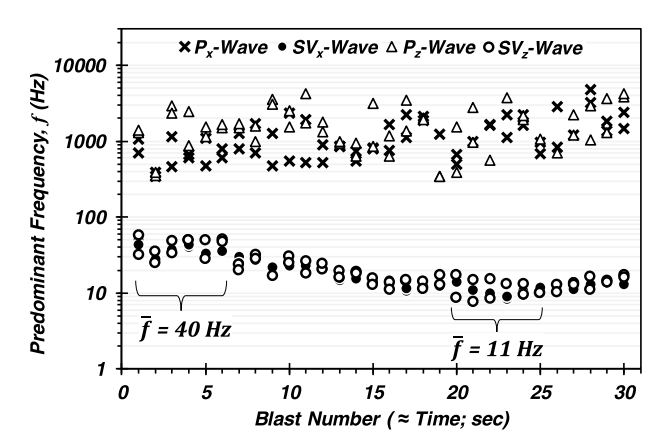


Fig. 8. Time-varying predominant frequency of P- and SV-waves during the DBP from two representative TGPs. Note that the predominant frequency SV_x -waves correspond to near-field effects, whereas those of SV_z -waves correspond to far-field shear waves.

Body Wave Dimensionality

Depending on the distance and the scale of observation, the waveforms produced by blasting may be considered 2D plane waves or 3D waves. Figs. 7(d–i) present V_z for vertically adjacent geophones within the same borehole to illustrate the amplitude and phase difference of body waves traversing the Sand Array during the blast programs. The amplitude and phase of the SV-waves recorded are nearly identical for many blasts [Figs. 7(d-1)], indicating planar shear wave fields at the scale of the Sand Array. Subtle differences between the SV-waves are attributed to slight differences in ray path distances, orientations of sensors, soil properties, and local diameter of the grout columns. A noticeable phase difference is observed for a detonation relatively proximate to the Sand Array [DBP Blast 30, Fig. 7(k)], and is indicative of a 3D wavefield. Because the use of the displacement-based method to calculate the shear strain does not require plane wave approximation (Cox 2006), it is used in the interpretation of the soil response regardless of wave dimensionality.

In Situ Dynamic Response to Controlled Blasting

Variation of Excess Pore Pressure with Shear Strain

Response of the Intact Sand Deposit

Fig. 9 presents the Sand Array response over the duration of the 8-s TBP, including the Cauchy shear strain, γ_{xz} , time-history within the two elements [Fig. 9(a)], and the corresponding γ_{oct} [Fig. 9(b)] and r_u [Fig. 9(c)] time-histories. Several blasts during the TBP exhibited a linear-elastic response, such as TBP Blast #1, which produced $\gamma_{xz,max} = 0.0002\%$, below the linear-elastic threshold shear strain, γ_{te} , and may be used to compute baseline elastic properties of the sand. The maximum γ_{xz} during the Test Blast Program was 0.0058% and 0.0071%, corresponding to $\gamma_{oct,max}$ equal to 0.0110% and 0.0104% for Elements 1 and 2, respectively. Whereas zero residual excess pore pressure was generated in Element 2 [Fig. 9(c)], the threshold shear strain to develop $u_{e,r}$ was observed in Element 1 with $r_{u,r} = 0.3\%$. Thus, the maximum shear strain produced during TBP Blast #8 (Table 1) exceeded both γ_{te} and γ_{tp} , where the latter appears to be equal to ~0.01% for the medium dense sand deposit in the undisturbed condition, similar to that reported by Dobry et al. (1982), Hsu and Vucetic (2004), Hazirbaba and Rathje (2009), and Dobry and

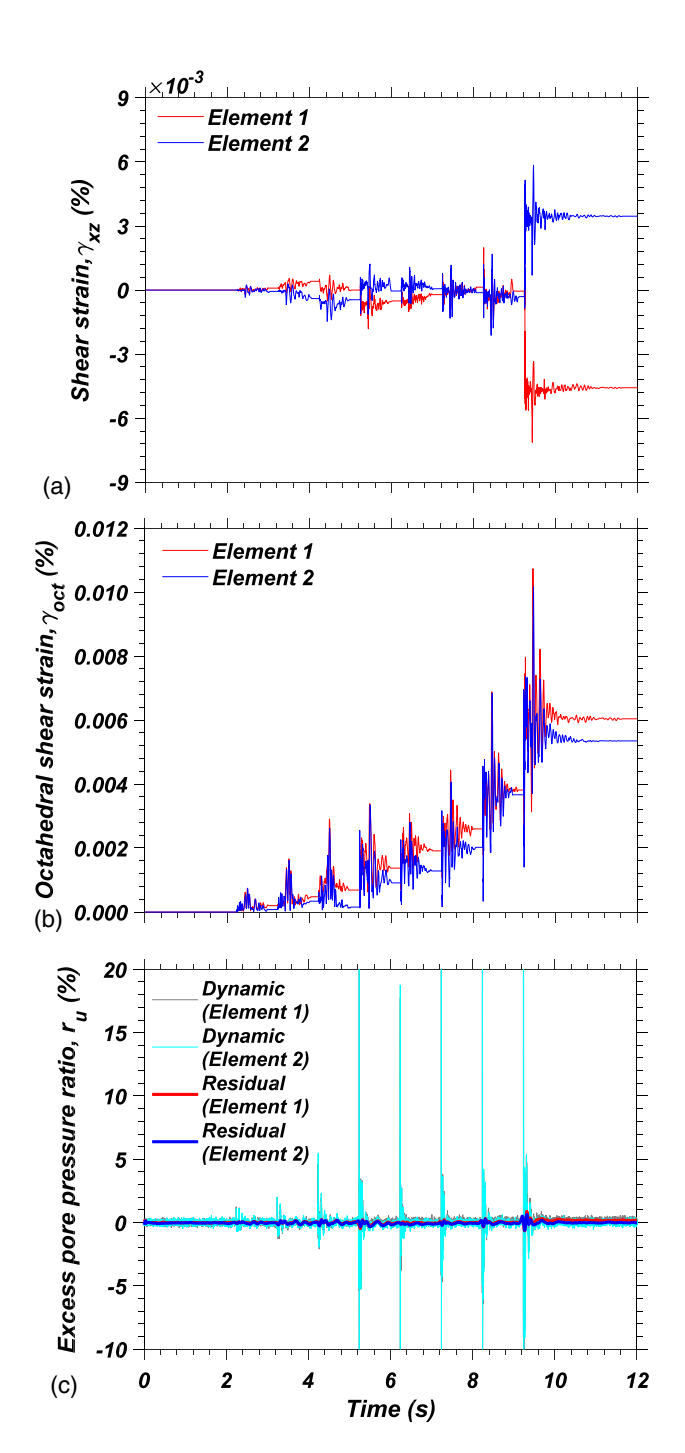


Fig. 9. Comparison of (a) Cauchy shear strain; (b) octahedral shear strain; and (c) excess pore pressure ratio time-histories in the Sand Array at Elements 1 (PPT-1) and 2 (PPT-4) during the TBP.

Abdoun (2015). Following the TBP, V_s in Elements 1 and 2 declined from 225 to 192 m/s, and 218 to 210 m/s (Table 2). The reduction in V_s in Element 1, on the order of 15%, appears correlated to the triggering of $u_{e,r}$, suggesting that subtle changes to the soil fabric occurred in Element 1 as a result of grain slippage and partial loss of grain-to-grain interlock. The change in V_s in Element 2 is considerably smaller, as no $u_{e,r}$ was triggered. The ground surface settlement survey performed after the test blast indicated remarkably uniform settlements across and transverse to the linear blast array of approximately 7 mm, representing very small volumetric strains within the sand deposit that could not serve to alter the geostatic stress state.

Table 2. Shear wave velocity, effective stresses, and estimated shear strain to trigger liquefaction for each blast program

Blast program	Vertical effective stress σ'_{vc} (kPa)	In situ shear wave velocity, V_s (m/s)	In situ normalized shear wave velocity, V_{s1} (m/s)	Reference shear strain ^a , γ_{r1} (%) (Darendeli 2001)	Reference shear strain ^b , γ_{r2} (%) (Menq 2003)	Threshold shear strain ^c , $\gamma_{cl,r1}$ (%)	Threshold shear strain ^d , $\gamma_{cl,r2}$ (%)
				Element 1			
Prior to TBP	256	225	178	0.042	0.066	0.139	0.071
Prior to DBP	256	192	151	0.042	0.066	0.087	0.054
Prior to SBP	83	167	175	0.028	0.042	0.053	0.036
				Element 2			
Prior to TBP	231	218	177	0.04	0.089	0.123	0.053
Prior to DBP	231	210	170	0.04	0.089	0.104	0.049
Prior to SBP	44	140	172	0.023	0.043	0.032	0.021

 $^{^{}a}\gamma_{r1}$ = reference shear strain derived using Darendeli (2001).

Fig. 10 presents several examples of γ_{xz} and r_u time-histories observed during the 30-s DBP, and indicates the accumulation of γ_{xz} and $r_{u,r}$ as detonated charges progressively became larger and closer to the Sand Array. The polarity of the maximum shear strain developed during passage of the near- and far-field SV-waves depended on the location (East vs. West) and depth of each charge relative to the array. The passage of each SV-wave is accompanied by a direct and corresponding variation of shear-induced u_e . For example, the γ_{xz} time-history for the 15th charge produces a variation in the SV-wave-induced r_u from 4% to 17%, and results in changes in $r_{u,r}$ from 6% and 5% to 9% and 8% for Elements 1 and 2, respectively. Although normal strains occur during passage of the SV-waves due to the lack of an imposed (i.e., artificial) drainage boundary condition, these normal strains are shear-induced and also occur during earthquake-induced shearing of natural soil deposits.

The Cauchy and octahedral shear strain and excess pore pressure ratio responses for Elements 1 and 2 are presented in Fig. 11 for the duration of the 30-s DBP. The accumulated Cauchy shear strain in Elements 1 and 2 reverses in azimuthal bearing (i.e., East vs. West) several times during the experiment [Fig. 11(a)]. This occurs as a result of differing charge weights detonating from differing depths (i.e., above, at, and below the TGP elevations) and azimuthal bearings to result in permanent shear strains. The maximum $|\gamma_{xz}|$ was 0.570% and 0.483% for Elements 1 and 2, respectively, resulting in a permanent accumulated γ_{xz} of 0.438% and 0.122%, respectively. Owing to its definition as a shear strain invariant, the permanent accumulated γ_{oct} is positive, and corresponds to 1.028% and 0.834% in Elements 1 and 2, respectively. Inspection of Figs. 11(a-c) reveals a direct relationship between γ_{xz} , γ_{oct} , and $r_{u,r}$, with increases in the rate of $r_{u,r}$ correlated to changes in the rate of shear strain accumulation. The maximum r_u and $r_{u,r}$ resulting from the Deep Blast Program was 73% and 57%, respectively, due to Blast #26 [Fig. 11(c)], at which time field drainage (i.e., dissipation of u_e) had already initiated under the established hydraulic gradients. This confirms that the in situ dynamic responses of sand deposits do not operate within an undrained condition, as postulated from recent centrifuge experiments of reconstituted sand (Adamidis and Madabhushi 2018; Ni et al. 2020; Abdoun et al. 2020).

The stress paths associated with blasting are different from that of common laboratory element tests such as the cyclic DSS test, which represent vertically propagating horizontal shear waves (i.e., assumed earthquake motions). Blast-induced particle motions are complex, and the predominant particle velocity is governed by the location and boundary condition associated with the energy

source—for example, the length of the charge relative to the scale of observation (Gohl et al. 2000; Blair 2010). The comparison of the mobilized maximum in situ γ with DSS test data is facilitated through the calculation of the DSS-equivalent, constant-volume shear strain, γ_{DSS} , which may be computed from γ_{oct} as follows (Cappa et al. 2017):

$$\gamma_{DSS} = \sqrt{\frac{3}{2}} \gamma_{oct} \tag{2}$$

which is strictly appropriate for 2D plane waves. Fig. 12 presents γ_{DSS} and r_u time-histories for selected blast pulses to demonstrate the identification of the maximum γ_{DSS} , $\gamma_{DSS,max}$, the in-shear $r_{u,max}$ observed during passage of SV-waves, and $r_{u,r}$ for comparison to shear strains across several orders of magnitude (e.g., Fig. 13). The use of 1-s detonation delays allowed for the straightforward selection of $r_{u,r}$ in the quiescent period in between successive charge detonations.

Fig. 13(a) presents the variation of $\gamma_{DSS,max}$ with $r_{u,max}$ observed within the Sand Array during the TBP, DBP, and SBP, and is compared with the response of previous laboratory element, large-scale, and centrifuge tests below. The $\gamma_{DSS,max}$ during the DBP is 1.371% and 1.200% for Elements 1 and 2, respectively. Note the following: (1) the initial (preblast) σ'_{vc} for Elements 1 and 2 was 256 and 231 kPa, respectively; and (2) the in situ observation of 2D shear strain of this magnitude and corresponding to these σ'_{vc} has not been previously reported. Fig. 13(b) presents the variation of $\gamma_{DSS,max}$ with $r_{u,r}$, and indicates that the initial γ_{tp} to produce $r_{u,r}$ ranges between 0.008% and 0.010% during the Test and Deep Blast Programs [Fig. 13(b) inset], consistent with the constant-volume, straincontrolled DSS tests on the reconstituted sand [Fig. 3(b); $\sigma'_{vc} =$ 240 kPa]. These in situ observations concur with previously reported γ_{tp} summarized by Dobry and Abdoun (2015) for laboratory element, centrifuge, large-scale laboratory, and field tests with $50 \le \sigma'_{v0} \le 200$ kPa. As the detonation sequence for the Deep Blast Program proceeded, $r_{u,r}$ accumulated rapidly for maximum shear strains greater than 0.01%, followed by a reduction in the rate of excess pore pressure generation as shear strain approached and exceeded 0.9% due to drainage under the local hydraulic gradients.

Response of Dynamically Strained and Unloaded Sand Deposit

Following dissipation of u_e generated from the DBP, bowl-shaped settlements of up to 120 mm manifested at the ground surface, and a volumetric strain, $\varepsilon_v = 1.2\%$, was measured over the depths of

 $^{{}^{\}rm b}\gamma_{r2}$ = reference shear strain derived using Menq (2003).

 $^{^{\}mathrm{c}}\gamma_{cl,r1}$ = cyclic shear strain needed to trigger liquefaction, derived using γ_{r1}

 $^{^{\}rm d}\gamma_{cl,r2}$ = cyclic shear strain needed to trigger liquefaction, derived using γ_{r2} .

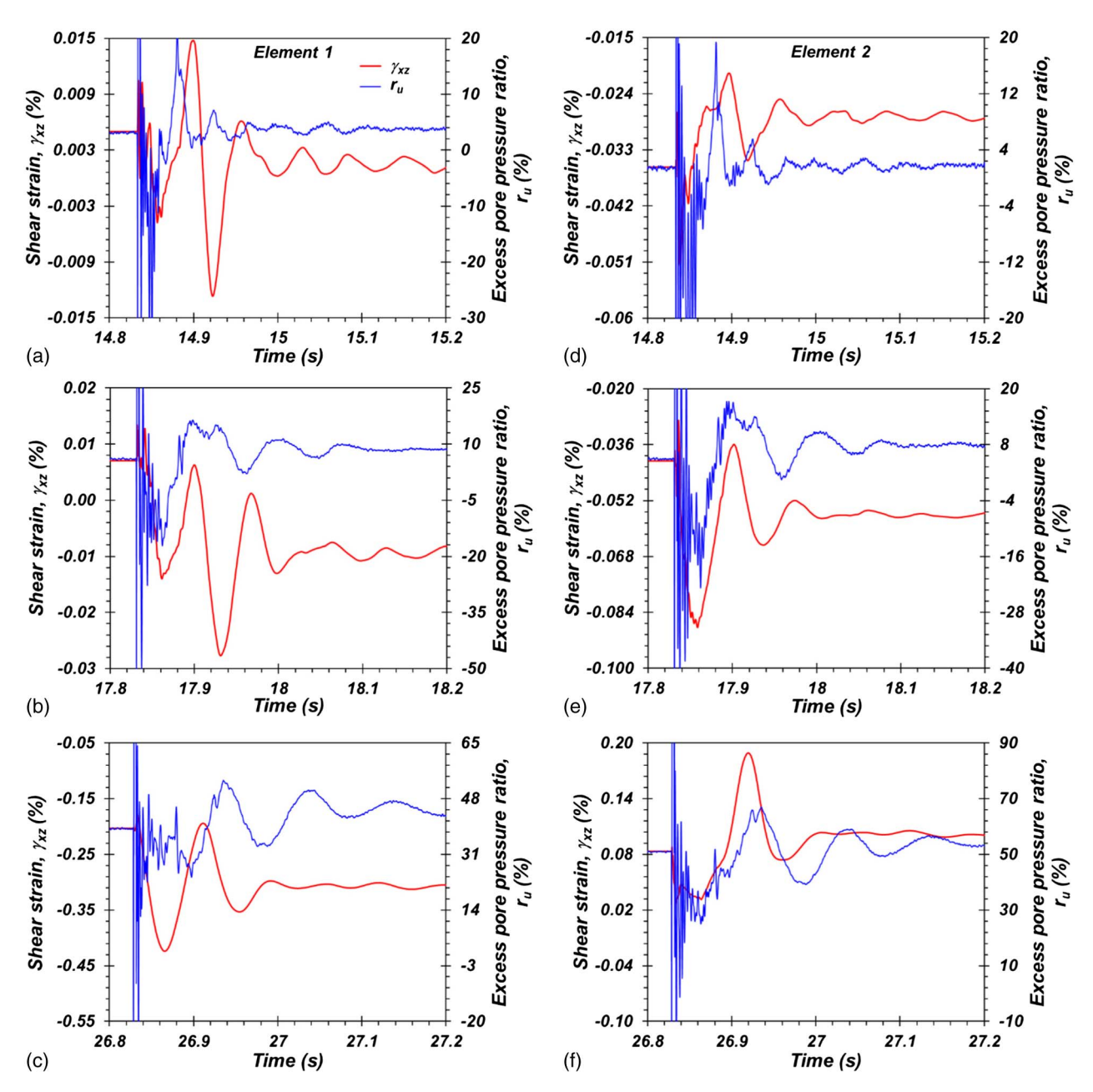


Fig. 10. Examples of Cauchy shear strain and corresponding excess pore pressure ratio time-histories for the Sand Array during the DBP: (a–c) Element 1 (PPT-1); and (d–f) Element 2 (PPT-4).

the Sand Array (Fig. 4) at inclinometer I-1 (Fig. 1). These deformations were accompanied with a large reduction in V_s within the Sand Array (Table 2) (Donaldson 2019). Space limitations prevent a detailed presentation of these phenomena; however, the reduction of V_s from 192 and 210 m/s to 167 and 140 m/s for Elements 1 and 2, respectively, immediately prior to the SBP (Table 2) and the observed bowl-shaped displacements point to the role of substantial changes to the soil fabric as a result of the large dynamic shear strains and subsequent reconsolidation (Mitchell and Solymar 1984), and stress arching (Gallant and Finno 2016; Mahvelati et al. 2020) to reduce σ'_{v0} in proximity to and within the Sand Array. The post-DBP V_s corresponds to $\sigma'_{vc} \approx$ 83 and 44 kPa, or a reduction in σ'_{vc} of 68% and 81% for Elements 1 and 2, respectively, estimated using the σ'_{vc} - V_s curve established from bender element tests of DSS test specimens of sand reconstituted from split-spoon samples [Fig. 3(b)]. The u_e response of the Sand Array during the SBP is interpreted in the framework of the new estimated stress state.

Fig. 14 presents γ_{xz} , γ_{oct} , and measured r_u time-histories in the Sand Array for Elements 1 and 2 observed during the SBP. The maximum shear-induced r_u and $r_{u,r}$ was 96% and 61%, respectively [Element 2; Figs. 13 and 14(c)], whereas the maximum γ_{oct} was 0.059% and 0.049% for Elements 1 and 2, respectively. The rate of $u_{e,r}$ generation in the sand during the Shallow Blast Program was noticeably greater than the two prior blast programs. The sand layer had experienced high residual excess pore pressures (i.e., $r_{u,r} = 57\%$) and large shear strains (i.e., $\gamma_{DSS,max} = 1.37\%$) the previous day, resulting in the resetting of the geological age of the deposit (e.g., Mitchell and Solymar 1984; Heidari and Andrus 2012; Mahvelati et al. 2020). The in situ shear strains were sufficiently large to alter the previously existing soil fabric, which had developed as a result of aging (e.g., creep) and a small amount

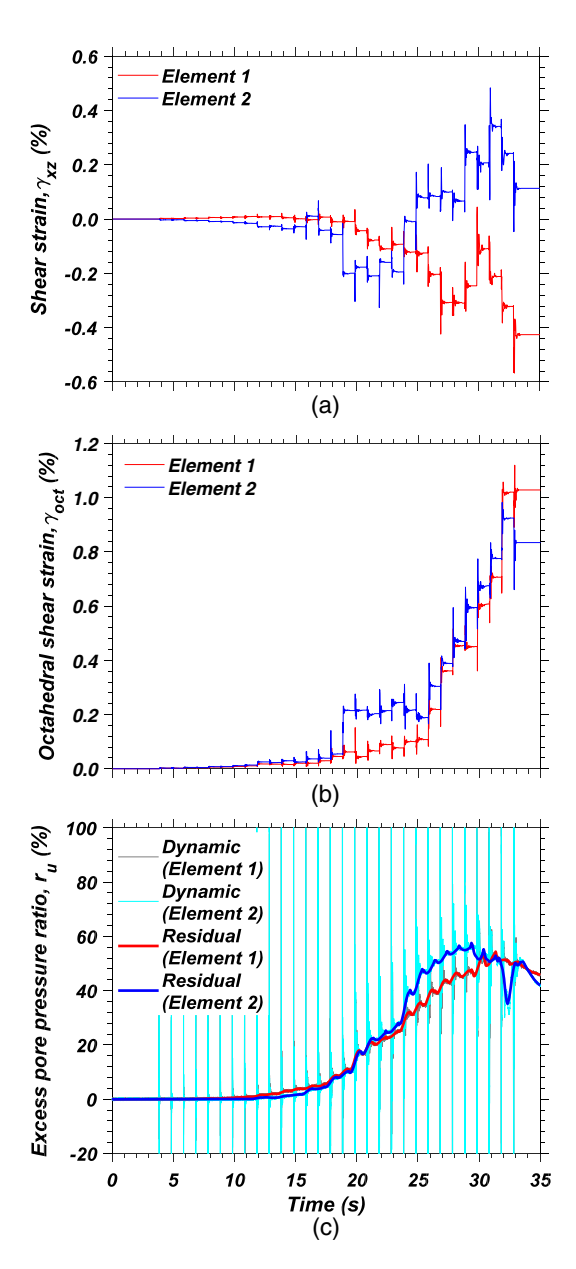


Fig. 11. Comparison of (a) Cauchy shear strain; (b) octahedral shear strain; and (c) excess pore pressure ratio time-histories in the Sand Array for Elements 1 (PPT-1) and 2 (PPT-4) during the DBP.

of cementation. The V_s in the Sand Array immediately prior to each blast program provides the basis for the interpretation of the changes in soil fabric resulting from each blast event (Table 2). The soil fabric in the Sand Array was slightly altered following the TBP in response to small-to-moderate shear strains (i.e., $\gamma_{oct} \approx$ 0.01%) that just approached and exceeded γ_{tp} in Elements 2 and 1, respectively, and represents the first of two distinct mechanisms responsible for the loss of small-strain stiffness. The largest reduction in V_s is associated with the in-shear tendency for contraction manifested as positive residual excess pore pressure [Element 1; Figs. 9 and 13(b)]. However, the shear strains experienced during the DBP fundamentally altered the soil fabric and stress state as manifested in the large reduction in V_s (Table 2) and the dynamic response of the Sand Array during the SBP (Fig. 14). In general, dissipation of pore pressure results in the densification of sand and corresponding increase in V_s (El-Sekelly et al. 2016b; Darby et al. 2019). The main difference between

previously reported mechanisms of soil fabric evolution and that observed herein results from the experimental method: the local 3D excess pore pressure field generated by controlled blasting resulted in the bowl-shaped settlement profile and corresponding stress arching, which should not occur following earthquakes in the absence of large local variation in relative density and shear stiffness. The settlement profile requires rotation of principle stresses at the ends of a "catenary" (the inflection of settlement curvature) to accommodate transfer of vertical stress in shear (Handy 1985), reducing the vertical stresses at depth, and providing the second of two mechanisms leading to the observed reduction in V_s as inferred from numerical simulations of mean effective stress acquisition associated with u_e dissipation by Gallant and Finno (2016). The increase in relative density of the sand in the Sand Array (estimated equal to 7%), associated with a local $\varepsilon_v = 1.2\%$, was strongly overshadowed by the sharp reduction in σ'_{v0} (Table 2) and change in the original soil fabric.

Role of Vertical Effective Stress on Generation of Excess Pore Pressure

Figs. 13(a and b) shows that the u_e response changed noticeably following the DBP as revealed during the SBP. The γ_{tp} reduced to 0.002%-0.003%, approximately one-quarter of that of the virgin, aged sand deposit [i.e., 0.008%-0.010%; Fig. 13(b) inset], similar to $\gamma_{tp} = 0.005\%$ reported by Chang et al. (2007) for a freshly deposited sand under $\sigma'_{v0} \approx 13$ kPa. Furthermore, the variation of shear-induced $r_{u,\text{max}}$ closely followed the $\gamma - r_{u,\text{max}}$ curve suggested by Dobry and Abdoun (2015) for large-scale and centrifuge tests of shallow (i.e., $\sigma'_{v0} \approx 24$ kPa) sand deposits. It is noteworthy that the $\gamma - r_{u,\text{max}}$ response of Element 1 $(\sigma'_{v0} \approx 83~\text{kPa})$ is less sensitive to shear strain than Element 2 $(\sigma'_{v0} \approx 44 \text{ kPa})$. Comparison of the sand response during the DBP (with $\sigma'_{v0} = 231$ and 256 kPa) to that during the SBP clearly indicates that increases in σ'_{v0} serve to shift the $\gamma - r_{u,\text{max}}$ and γ – $r_{u,r}$ responses to the right (i.e., shear strain increases for a given r_u). Additional comparison of the SBP and DBP $\gamma_{DSS,max} - r_{u,max}$ and $\gamma_{DSS,max} - r_{u,r}$ responses to that of shallow in situ measurements reported by Cox (2006) (Figs. S1 and S2) and Chang et al. (2007) Figs. S3 and S4) are provided in the Supplemental Materials, and further support the evidence of significant reduction in σ'_{v0} following the DBP and that such $\gamma - r_{u,r}$ responses are pressuredependent. These in situ test results serve to confirm the role of effective overburden pressure on the $\gamma - r_{u,\text{max}}$ responses summarized by Ni et al. (2021) for large-scale and centrifuge tests on reconstituted sands. In addition to the resetting of the geologic age of the deposit and the degradation of cementation, raised excess pore pressures tend to migrate upward in response to the induced hydraulic gradient, causing a loss of effective stress, and therefore a reduction in strength and increase in compressibility, which may have lowered the liquefaction resistance of the sand in response to the next dynamic event (El-Sekelly 2016a; Dobry et al. 2015; Cubrinovski et al. 2018). Unfortunately, the use of a single vertical PPT string set within a 3D excess pore pressure field cannot adequately capture the resulting hydraulic gradients and possible horizontal drainage that likely contributed to pore pressure dissipation. Nonetheless, it is possible that the large straining and flow of pore water provided by the DBP, and certainly the loss of σ'_{v0} , served to reduce the soil resistance to liquefaction in the Sand Array during the SBP.

Comparison with Laboratory Test-Based Excess Pore Pressure–Shear Strain Relationships and Cyclic Strain for Liquefaction

Fig. 13(a) compares the Sand Array responses to the average maximum u_e response for $D_r = 51\%$ derived from 185 stress-controlled

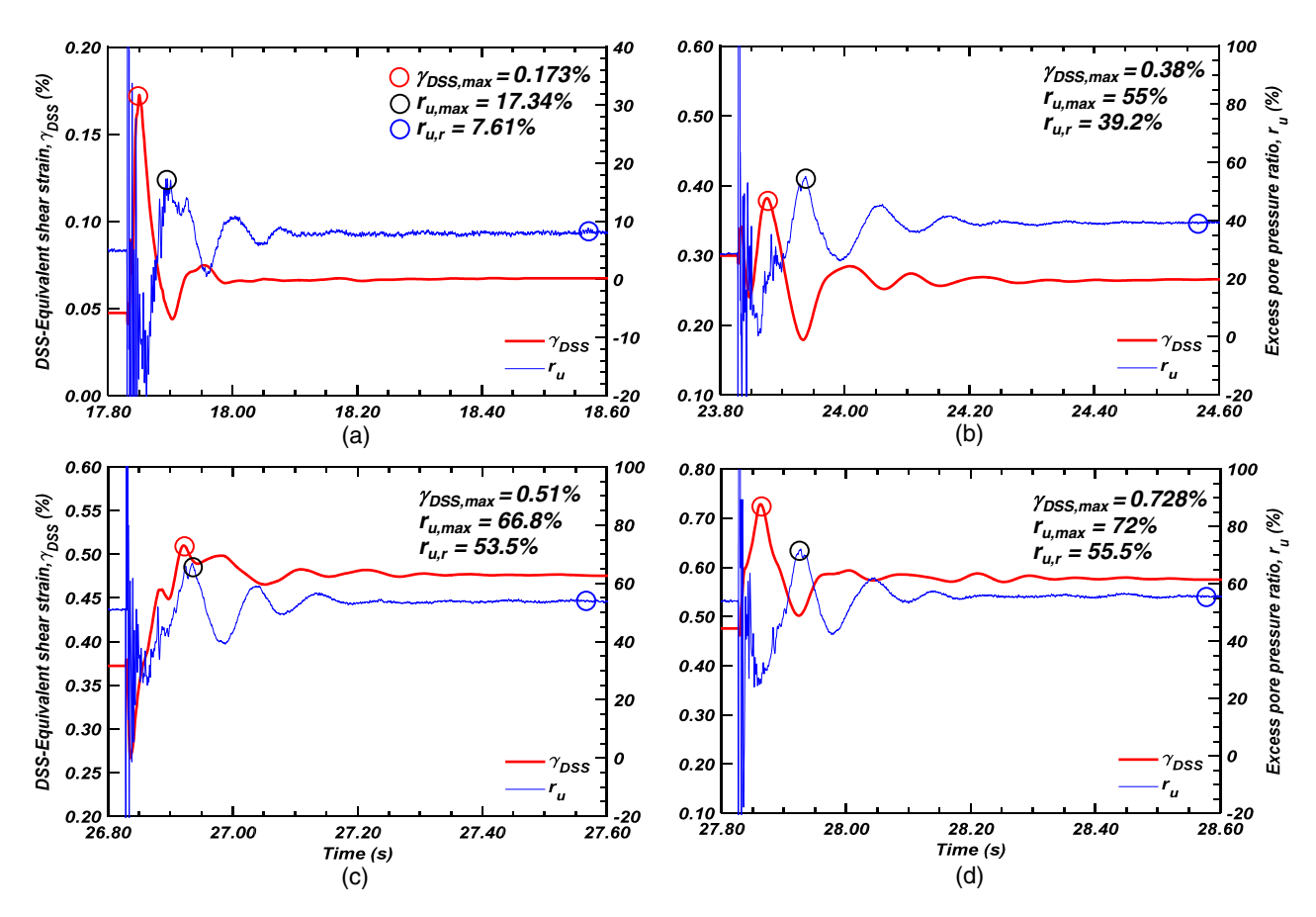


Fig. 12. Examples of DSS-equivalent shear strain and excess pore pressure time-histories from Element 2 demonstrating the identification of $\gamma_{DSS,max}$, $r_{u,max}$, and $r_{u,r}$: (a) Blast #15; (b) Blast #21; (c) Blast #24; and (d) Blast #25.

cyclic DSS and triaxial tests reported by Cetin and Bilge (2012) [Fig. 13(a)]. The Cetin and Bilge (2012) curve significantly overestimates the shear strain for a given magnitude of $r_{u,\text{max}}$. In addition to those factors related to the field behavior identified below, the deviation in responses may result from the greater sensitivity of excess pore pressure to cyclic strain, rather than cyclic stress as described by Dobry et al. (1982) and Dobry and Abdoun (2015, 2017). For example, Fig. 13(b) presents the $\gamma_{DSS, max} - r_{u,r}$ responses observed in the various blast programs to the constantvolume strain-controlled DSS tests conducted on reconstituted specimens ($\sigma'_{vc} = 240 \text{ kPa}$) derived from the split-spoon samples retrieved from the Sand Array. Although the agreement in shear strain-excess pore pressure responses are better for the straincontrolled tests than those anticipated from stress-controlled tests, the response of the Sand Array generally indicates greater $u_{e,r}$ than the reconstituted DSS test specimens for a given $\gamma_{DSS,max}$ in the range of ~\%0.1 to 0.8\%. Deviations between the laboratory and in situ observations could result from (1) the effect of multidirectional ground motions imposed on the Sand Array, (2) the effect of the natural soil fabric developed over thousands of years of aging, (3) the redistribution and upward migration of the excess pore pressure that has been postulated to occur in the field during earthquakes (Cubrinovski et al. 2019), or (4) a combination of these three phenomena, none of which are readily simulated in the laboratory. At larger strains (e.g., greater than 0.8%), the laboratory testbased $r_{u,r}$ response derived from the strain-controlled DSS tests indicates continued generation of excess pore pressure to liquefaction (i.e., $r_{u,r} = 1.0$) due to the imposed constant-volume boundary condition.

Table 2 summarizes the estimated threshold shear strain required to trigger liquefaction, γ_{cl} , based on the small-strain V_s using the methodology developed by Dobry and Abdoun (2015) for a $M_w = 7.5$ earthquake scenario. The calculated γ_{cl} for the V_s corresponding to the onset of the DBP is smaller than that observed, which could be attributed to the partial drainage observed during the in situ dynamic test or the lack of correspondence to an $M_w =$ 7.5 earthquake. Recent observations derived from centrifuge tests indicate that partial drainage serves to increase the liquefaction resistance of the sand deposit at a higher confining pressure due to pressure-dependency of the coefficient of consolidation (Ni et al. 2020; Abdoun et al. 2020). However, the calculated γ_{cl} for the freshly deposited sand under much lower σ'_{v0} at the onset of the SBP is similar to that measured in situ. Thus, these experiments demonstrate that liquefaction manifests under γ_{cl} smaller than those suggested by the cyclic stress approach, and that liquefaction triggering is a highly stress-dependent phenomenon, as noted by many others. Further efforts presently underway seek to clarify these observations through the lens of the overburden stress correction factor, K_{σ} .

Shear Modulus Degradation with Shear Strain

Response of the Intact Sand Deposit

The crosshole shear wave velocity within the Sand Array was calculated using the time separating far-field SV-waves for each of the laterally offset TGP pairs and the ray path distance to facilitate computation of the change in G with shear strain amplitude. Since the elevation of each charge and TGP were not necessarily shared,

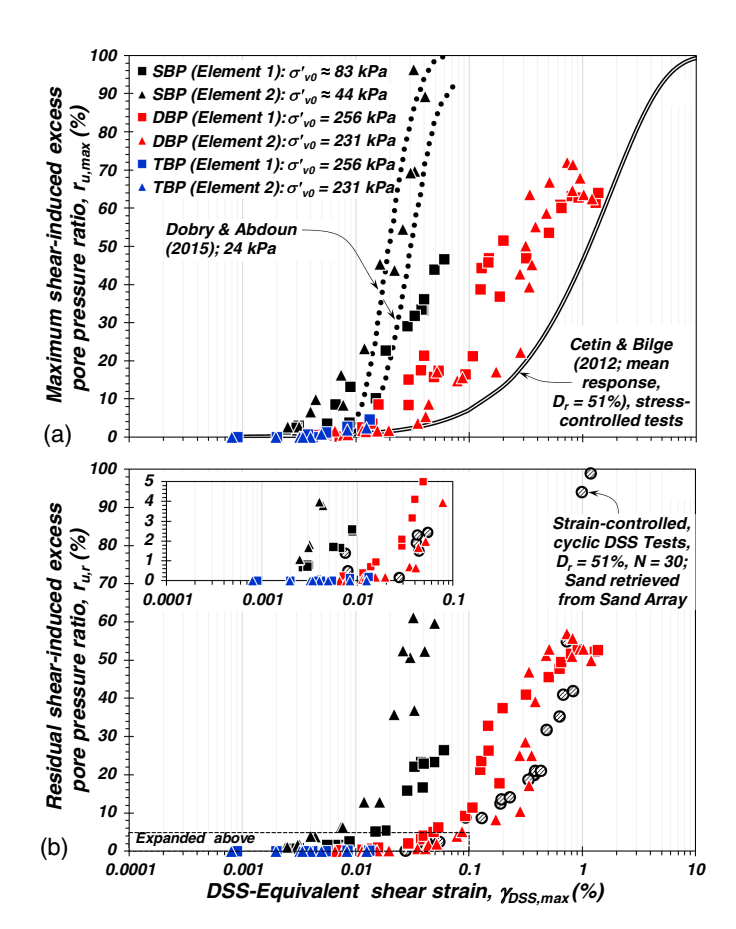


Fig. 13. Excess pore pressure–shear strain responses from the TBP, DBP, and SBP: (a) variation maximum shear-induced excess pore pressure ratio with maximum DSS-equivalent shear strain; and (b) variation of residual shear-induced excess pore pressure ratio with maximum DSS-equivalent shear strain.

the direct linear ray path distance from the center of each charge (Heelan 1953) to each TGP was used to calculate V_s . The estimated arrival time of the far-field SV-wave was estimated using the ray path distance, crosshole V_p , and the initial or antecedent crosshole V_s [Fig. 15(a)]. The arrival times were cross-checked using the normalized Stockwell spectrogram [Fig. 15(b)] constructed using the vertical (e.g., TGP S13z) velocity time-history following the procedures described by Kramer et al. (2016), and were indicated by the shift in predominant frequency of the ground motion. Fig. 15(b) clearly shows the frequency content of the P-wave; the near-field SV-wave, which exhibited intermittent high-frequency components superimposed upon the lower-frequency backbone signal; and the delayed arrival of the strain-dependent far-field SV-wave.

Figs. 15(c and d) illustrate examples of the time delay between SV-waves recorded in TGP pair S10 and S13. The strain-dependent V_s resulting from each blast in the Test and Deep Blast Programs and corresponding shear modulus reduction characteristics are presented in Fig. 16 in terms of $\gamma_{DSS,max}$. Fig. 16(a) demonstrates that (1) the linear-elastic regime was maintained through $\gamma_{DSS,max} \approx 0.001\%-0.002\%$, based on the lack of scatter in V_s in this range of shear strain; and (2) the linear-elastic threshold shear strain, γ_{te} , was exceeded to demonstrate observable nonlinearity during the relatively small excitation of the TBP [Table 1; Figs. 7(a) and 9]. The crosshole V_s corresponding to the linear-elastic shear strain was used as the basis for determining the shear modulus reduction characteristics for data derived from the TBP.

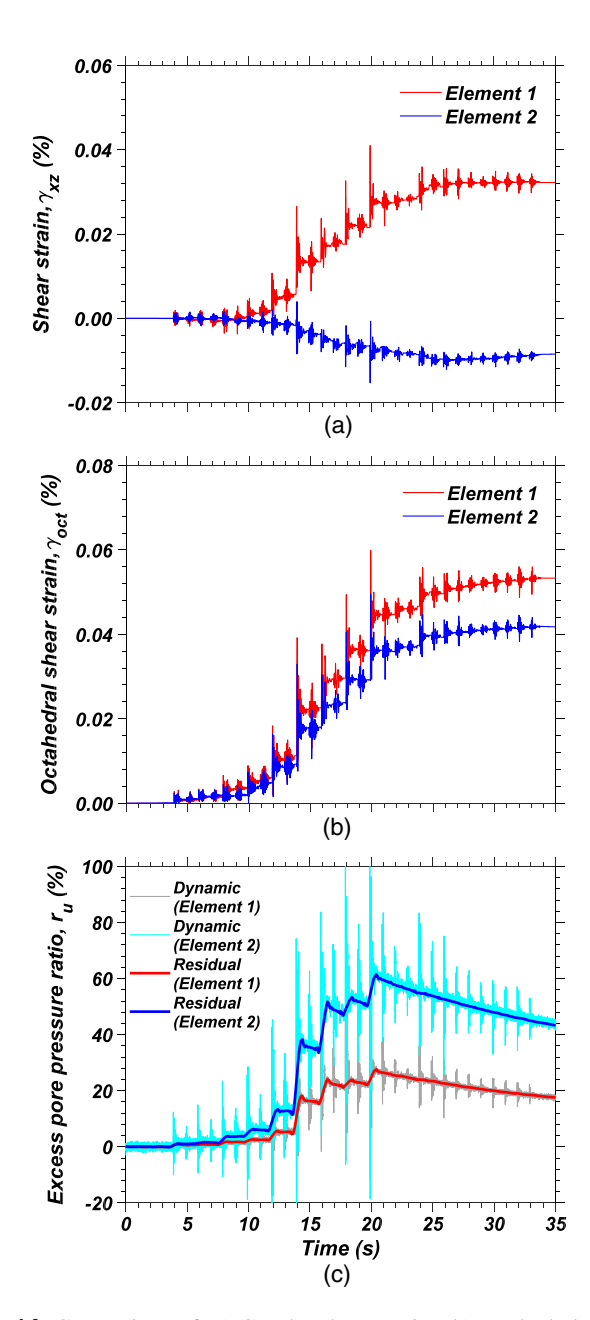


Fig. 14. Comparison of (a) Cauchy shear strain; (b) octahedral shear strain; and (c) excess pore pressure ratio time-histories in the Sand Array for Elements 1 (PPT-1) and 2 (PPT-4) during the SBP.

Downhole tests conducted prior to each blast program served to provide the small strain V_s and shear modulus, $G_{\rm max}$, within the Sand Array, and was used to normalize $G/G_{\rm max}$ for the DBP (Table 2), where G was computed using

$$G = \rho V_s^2 \tag{3}$$

where ρ = soil density, estimated equal to 1,900 kg/m³ within the Sand Array. The average initial $G_{\rm max}$ for Elements 1 and 2 were equal to 99 and 92 MPa, and 71 and 85 MPa, for the Test and Deep Blast Programs, respectively. Fig. 16(b) presents the variation of V_s with $\gamma_{DSS,{\rm max}}$ and indicates a reduction from the pre-DBP average of 196 m/s to about 75 m/s over the 30-s Deep Blast Program, with $\gamma_{DSS,{\rm max}}$ spanning four orders of magnitude. The large reduction in V_s corresponds to the development of significant

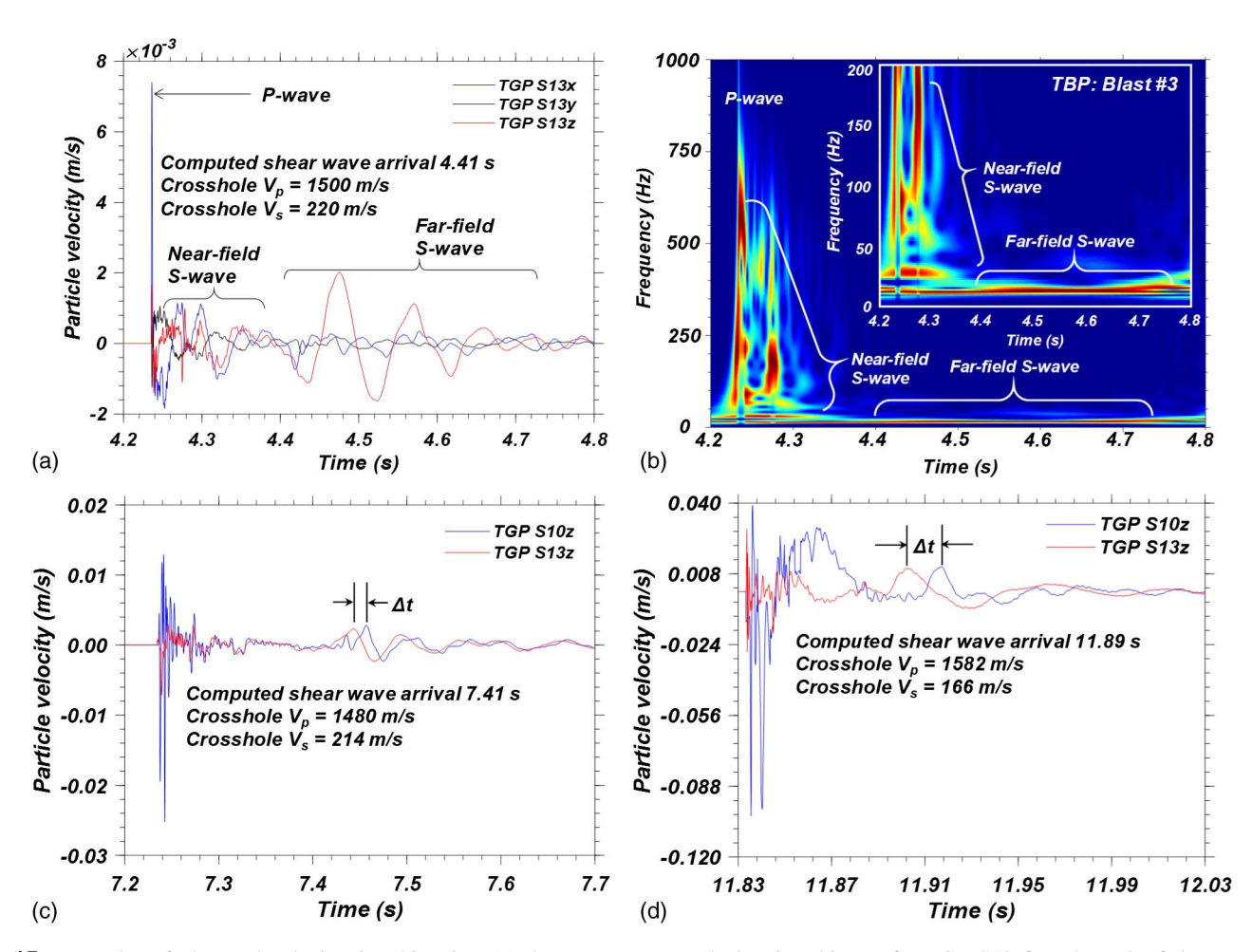


Fig. 15. Examples of observed velocity time-histories: (a) three-component velocity time history for TGP S13 for Blast #3 of the TBP; and (b) corresponding normalized Stockwell spectrogram, both of which illustrate the *P*-wave arrival, near-field *S*-waves due to local shearing associated with unloading of the *P*-wave, and far-field *S*-wave generated at the source. Comparison of the shear (*SV*) wave amplitudes and phases of two horizontally separated geophones located within different boreholes for (c) TBP Blast #6; and (d) DBP Blast #9 observed in TGPs 10 and 13.

nonlinearity and, considering the u_e generated (Fig. 11), demonstrable excitation in the nonlinear-inelastic regime.

Fig. 16(c) presents the variation of $G/G_{\rm max}$ with $\gamma_{DSS,{\rm max}}$ for the TBP and DBP (n.b., significantly inclined ray paths prevented reliable calculation of V_s during the SBP). Comparison of Figs. 16(c) and 13(b) indicates that $\gamma_{tp}=0.01\%$ and initiation of u_e corresponds to $G/G_{\rm max}=0.70+/-0.08$, similar to previous observations conducted at significantly shallower depths (e.g., Roberts et al. 2016). The use of normalized G appears to satisfactorily capture stress-dependent variations in stiffness-related constitutive soil responses. As $\gamma_{DSS,{\rm max}}$ exceeds ~0.1%, the observed normalized shear modulus exhibited greater linearity than expected from laboratory-based $G/G_{\rm max}$ responses proposed by Seed and Idriss (1970) and Menq (2003), due to the initiation of drainage during the excitation.

Comparison with Laboratory Test-Based G/G_{max} Relationships

Interpretation of the observed $G/G_{\rm max}$ data within the framework of laboratory tests on reconstituted sand specimens suggests that γ_{te} is 0.001%–0.002% [Fig. 16(c)], compared with 0.0008% expected from $G/G_{\rm max}$ curves derived by Menq (2003). Such a comparison is appropriate in view of the frequency content of the blast-induced S-waves, indicating that corrections for strain rate may not be necessary. Scatter in experimental data presented herein indicates that γ_{te} from reconstituted specimens may provide a

suitable, if conservative, estimate of the in situ threshold in linearelastic constitutive response. The G/G_{max} at intermediate strains corresponding to the nonlinear-elastic constitutive regime are likewise suitably captured. However, at large strains, the constantvolume laboratory-based G/G_{max} depart from that observed in situ as a result of the drainage initiated under the established hydraulic gradients, which serves to maintain a larger shear stiffness within the Sand Array under continuing dynamic excitation. The implications for this observation relate to the possibility of drainage contributing to smaller amplification of longer period, and greater amplification of shorter period motions during long-duration earthquakes (e.g., subduction zone earthquakes). The consequences of drainage on the system response of deep liquefiable deposits during long-duration events may be investigated using coupled nonlinear time domain analyses such as those reported by Cubrinovski et al. (2019).

Concluding Remarks

Three controlled blasting experiments were conducted to observe the in situ dynamic response of a liquefiable, medium dense sand deposit using triaxial geophones and excess pore pressures forming an instrumented array, termed the Sand Array, and placed at an average depth of 25 m. Designated the Test (8 s), Deep, (30 s), and Shallow (30 s) Blast Programs, these experiments provided

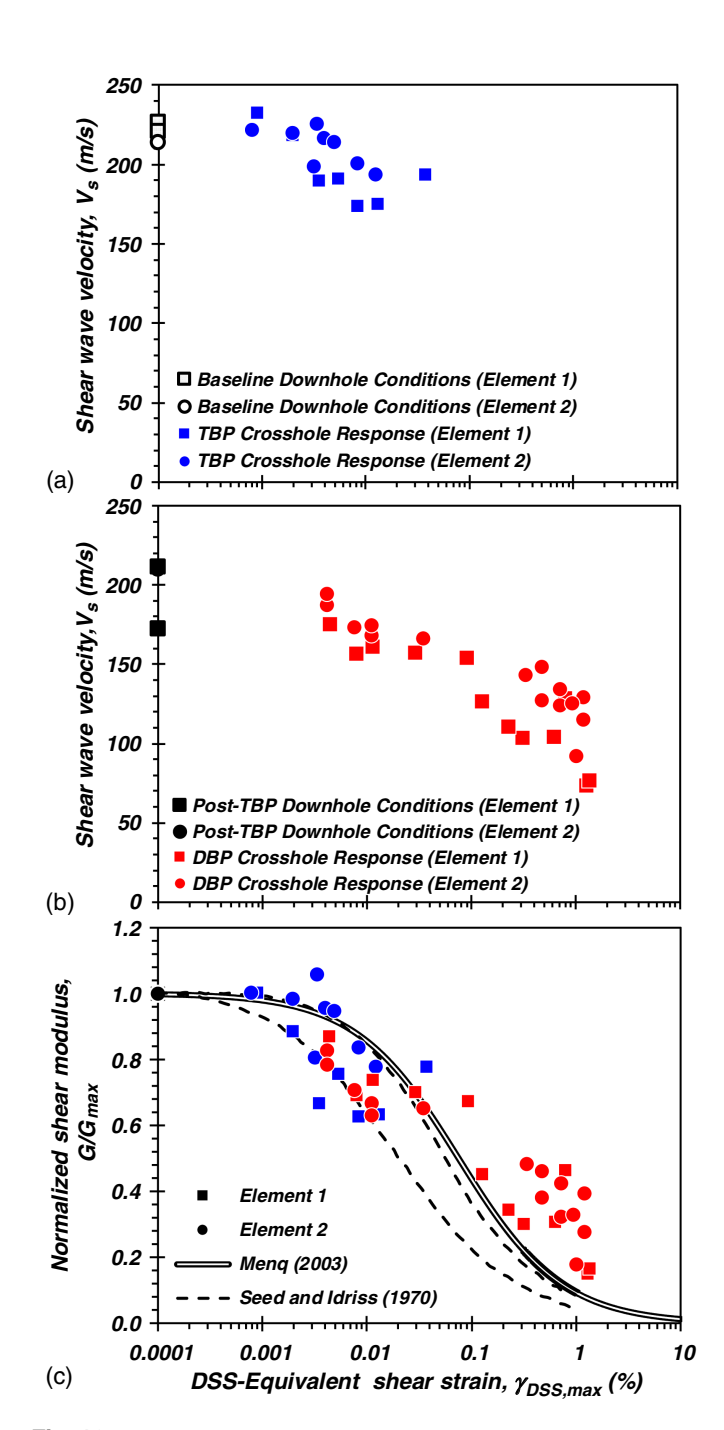


Fig. 16. Variation of shear wave velocity with shear strain in the Sand Array as observed during (a) TBP, and (b) DBP; and (c) corresponding normalized shear modulus degradation with shear strain.

the basis to examine the in situ dynamic responses of a natural and subsequently redeposited sand under high effective overburden stresses, σ'_{v0} , without the limitations inherent in the laboratory investigation of such responses. In addition to providing a detailed characterization of blast-induced ground motions and the corresponding coupled fluid-mechanical interaction, these experiments facilitated a comprehensive evaluation of the dynamic constitutive response of the deep sand deposit, and demonstrated the suitability of such experiments for the dynamic characterization of geological materials. Based on the results of the suite of in situ tests, the main conclusions are as follows:

1. The frequency content of *P*-waves is sufficiently large to prevent large particle displacements, strains, or generation of

- residual excess pore pressure. Blast-induced *P*-waves pass in a drained state and do not dominate the displacement, strain, or excess pore pressure response for the source-to-site distances evaluated.
- 2. The frequency content of blast-induced *SV*-waves lies within the range of earthquake ground motions, and corrections for strain rate do not appear necessary.
- 3. The linear-elastic threshold shear strain, γ_{te} , of the natural intact sand deposit ranged from 0.001% to 0.002%, slightly larger than expected from resonant column-torsional shear tests on reconstituted sand specimens. The threshold shear strain to initiate the generation of excess pore pressure, γ_{tp} , ranged from 0.008% to 0.010%, and are broadly consistent with previously reported threshold strains and confirms the apparent independence of γ_{tp} on effective overburden stress for $50 \le \sigma'_{v0} \le 250$ kPa.
- 4. Maximum excess pore pressures were significantly larger in situ than those associated with stress-controlled cyclic laboratory tests for a given shear strain. Residual excess pore pressures observed in situ were somewhat larger than those derived from strain-controlled, cyclic direct simple shear tests on the reconstituted sand. These observations stem from the greater sensitivity of excess pore pressure to shear strain than from shear stress, the effects of multidirectional shaking and existing natural soil fabric, and the redistribution of excess pore pressure.
- 5. The relatively small Test Blast Program appears to have produced subtle changes in soil fabric as deduced from the changes in shear wave velocity within the Sand Array. The dynamic excitation provided by the significantly larger Deep Blast Program appears to have reset the geological age of the sand deposit as a consequence of the large strains imposed. Reductions in shear wave velocity following this dynamic event were significant, pointing to the change in soil fabric and reduction in σ'_{v0} associated with stress arching, which occurred as a consequence of the dissipation of the 3D excess pore pressure field.
- 6. The rate of excess pore pressure generation in the redeposited sand was greater than that observed for the natural intact sand deposit, with γ_{tp} ranging from 0.002% to 0.003%, approximately one-quarter of that for the natural sand deposit. Redistribution of excess pore pressure and large straining during, and reduction in σ'_{v0} following, the Deep Blast Program served to lower the liquefaction resistance of the sand in response to the subsequent Shallow Blast Program, confirming previous laboratory and large-scale experiments and postulated from post-earthquake reconnaissance observations.
- 7. The Deep and Shallow Blast Programs confirm recent large-scale and centrifuge test data, which suggest that increases in σ'_{v0} serve to shift the shear strain–excess pore pressure relationship from smaller to larger shear strains.
- 8. Reductions in shear modulus of approximately $0.70G_{\rm max} + / 0.08G_{\rm max}$ appear necessary prior to the triggering of residual excess pore pressure in the intact natural sand deposit. Drainage appears to have contributed to a stiffer large-strain response than otherwise expected from laboratory-derived shear modulus reduction curves, and this phenomenon may pose significant consequences for long-duration earthquakes.

In addition to these observations, it may be concluded that controlled blasting experiments such as those described herein can be used to determine fundamental dynamic properties of any kind of soil, are particularly well-suited for soils that are not easily sampled, and can be conducted at any depth, thereby providing a new avenue for determining vital dynamic characteristics of geological materials.

Data Availability Statement

Some or all data, models, or code that support the findings of this study are available from the corresponding author upon reasonable request.

Acknowledgments

The authors gratefully acknowledge the sponsorship of this work by Cascadia Lifelines Program (CLiP) and its members, with special thanks to member agency Port of Portland. The authors were supported by the National Science Foundation (Grant No. CMMI 1663654) on similar work during the course of these experiments. This research was encouraged and facilitated by Tom Wharton, P.E., of the Port of Portland. We thank Jason Bock, P.E., of GeoResources, Inc. for coordination of the initial screening of test sites. The authors thank Mike Gomez, University of Washington, for the calcium carbonate content determination, and Jordan Melby, P.E., of GeoDesign, Inc., Dr. Seth C. Reddy, P.E., of GeoResources, Inc., and Robert Miner, P.E., of RMDT, Inc., for assisting with energy measurements during standard penetration testing. Thanks are due to T. Matthew Evans, Anne Trehu, James Batti, Aleyna Donaldson, Erick Moreno-Rangel, and Ali Dadashi for engaging in discussions and/or assistance with various portions of the overall project. The authors thank Kenneth H. Stokoe II, Brady R. Cox, Farnyuh Menq, Benchen Zhang, Ricardo Dobry, Tarek Abdoun, and Waleed El-Sekelly for fruitful discussions related to this work. The authors are grateful to the anonymous reviewers for their thoughtful comments and suggestions.

Supplemental Materials

Figs. S1–S4 are available online in the ASCE Library (www ascelibrary.org).

References

- Abdoun, T., M. Ni, R. Dobry, K. Zehtab, A. Marr, and W. El-Sekelly. 2020. "Pore pressure and K_{σ} evaluation at high overburden pressure under field drainage conditions. II: Additional interpretation." *J. Geotech. Geoenviron. Eng.* 146 (9): 04020089. https://doi.org/10.1061/(ASCE)GT.1943-5606.0002302.
- Adamidis, O., and S. P. G. Madabhushi. 2018. "Experimental investigation of drainage during earthquake-induced liquefaction." *Géotechnique* 68 (8): 655–665. https://doi.org/10.1680/jgeot.16.P.090.
- Amoroso, S., K. M. Rollins, P. Andersen, G. Gottardi, L. Tonni, M. F. G. Martínez, and P. M. De Martini. 2020. "Blast-induced liquefaction in silty sands for full-scale testing of ground improvement methods: Insights from a multidisciplinary study." *Eng. Geol.* 265 (Feb): 105437. https://doi.org/10.1016/j.enggeo.2019.105437.
- Andrus, R. D., H. Hayati, and N. P. Mohanan. 2009. "Correcting liquefaction resistance of aged sands using measured to estimated velocity ratio." *J. Geotech. Geoenviron. Eng.* 135 (6): 735–744. https://doi.org/10.1061/(ASCE)GT.1943-5606.0000025.
- Ashford, S. A., K. M. Rollins, and J. I. Baez. 2000a. "Comparison of deep foundation performance in improved and non-improved ground using blast-induced liquefaction." In *Soil dynamics and liquefaction*, 20–34. Reston, VA: ASCE.
- Ashford, S. A., K. M. Rollins, S. C. Bradford, T. J. Weaver, and J. I. Baez. 2000b. "Liquefaction mitigation using stone columns around deep foundations: Full-scale test results." *Transp. Res. Rec.* 1736 (1): 110–118. https://doi.org/10.3141/1736-14.
- Ashford, S. A., K. M. Rollins, and J. D. Lane. 2004. "Blast-induced lique-faction for full-scale foundation testing." J. Geotech. Geoenviron. Eng.

- 130 (8): 798–806. https://doi.org/10.1061/(ASCE)1090-0241(2004) 130:8(798).
- Ashmawy, A. K., B. Sukumaran, and V. Vinh Hoang. 2003. "Evaluating the influence of particle shape on liquefaction behavior using discrete element modelling." In *Proc.*, 13th Int. Offshore and Polar Engineering Conf. 542–549, Honolulu: International Society of Offshore and Polar Engineers.
- ASTM. 2014. Standard test method for EST method for rapid determination of carbonate content of soils. ASTM D4373-14. West Conshohocken, PA: ASTM.
- Biot, M. A. 1956a. "Theory of propagation of elastic waves in a fluid saturated porous solid. 1. Low frequency range." J. Acoust. Soc. Am. 28 (2): 168–178. https://doi.org/10.1121/1.1908239.
- Biot, M. A. 1956b. "Theory of propagation of elastic waves in a fluid saturated porous solid. 2. Higher frequency range." J. Acoust. Soc. Am. 28 (2): 179–191. https://doi.org/10.1121/1.1908241.
- Blair, D. P. 2007. "A comparison of Heelan and exact solutions for seismic radiation from a short cylindrical charge." *Geophysics* 72 (2): 33–41. https://doi.org/10.1190/1.2424543.
- Blair, D. P. 2010. "Seismic radiation from an explosive column." Geophysics 75 (1): 55–65. https://doi.org/10.1190/1.3294860.
- Boulanger, R. W., and I. M. Idriss. 2014. CPT and SPT based liquefaction triggering procedures. Rep. No. UCD/CGM.-14. Davis, CA: Univ. of California.
- Boulanger, R. W., and I. M. Idriss. 2016. "CPT-based liquefaction triggering procedure." *J. Geotech. Geoenviron. Eng.* 142 (2): 04015065. https://doi.org/10.1061/(ASCE)GT.1943-5606.0001388.
- Campbell, K. W., and Y. Bozorgnia. 2008. "NGA ground motion model for the geometric mean horizontal component of PGA, PGV, PGD and 5% damped linear elastic response spectra for periods ranging from 0.01 to 10 s." *Earthquake Spectra* 24 (1): 139–171. https://doi.org/10.1193/1 .2857546.
- Cappa, R., S. J. Brandenberg, and A. Lemnitzer. 2017. "Strains and pore pressures generated during cyclic loading of embankments on organic soil." *J. Geotech. Geoenviron. Eng.* 143 (9): 04017069. https://doi.org /10.1061/(ASCE)GT.1943-5606.0001721.
- Cetin, K. O., and H. T. Bilge. 2012. "Cyclic large strain and induced pore pressure models for saturated clean sands." *J. Geotech. Geoenviron. Eng.* 138 (3): 309–323. https://doi.org/10.1061/(ASCE)GT.1943 -5606.0000631.
- Chang, W. J., E. M. Rathje, K. H. Stokoe, and K. Hazirbaba. 2007. "In situ pore pressure generation behavior of liquefiable sand." *J. Geotech. Geoenviron. Eng.* 133 (8): 921–931. https://doi.org/10.1061/(ASCE)1090-0241(2007)133:8(921).
- Charlie, W. A., T. E. Bretz, L. A. Schure, and D. O. Doehring. 2013. "Blast-induced pore pressure and liquefaction of saturated sand." *J. Geotech. Geoenviron. Eng.* 139 (8): 1308–1319. https://doi.org/10.1061/(ASCE) GT.1943-5606.0000846.
- Charlie, W. A., D. O. Doehring, G. E. Veyera, and H. A. Hassen. 1988. Blast induced liquefaction of soils: Laboratory and field tests. Washington, DC: Air Force Office of Scientific Research.
- Charlie, W. A., P. J. Jacobs, and D. O. Doehring. 1992. "Blast induced liquefaction of an alluvial sand deposit." *Geotech. Test. J.* 15 (1): 14–23. https://doi.org/10.1520/GTJ10220J.
- Cox, B. R. 2006. "Development of a direct test method for dynamically assessing the liquefaction resistance of soils in situ." Ph.D. dissertation, Dept. of Civil, Architectural, and Environmental Engineering, Univ. of Texas at Austin.
- Cox, B. R., K. H. Stokoe, and E. M. Rathje. 2009. "An in-situ test method for evaluating the coupled pore pressure generation and nonlinear shear modulus behavior of liquefiable soils." *Geotech. Test. J.* 32 (1): 11–21. https://doi.org/10.1520/GTJ101484.
- Cubrinovski, M., and K. Ishihara. 1999. "Empirical correlation between SPT N-value and relative density for sandy soils." *Soils Found.* 39 (5): 61–71. https://doi.org/10.3208/sandf.39.5_61.
- Cubrinovski, M., A. Rhodes, N. Ntritsos, and S. Van Ballegooy. 2019.
 "System response of liquefiable deposits." Soil Dyn. Earthquake Eng. 124 (Sep): 212–229. https://doi.org/10.1016/j.soildyn.2018.05.013.

- Darby, K. M., R. W. Boulanger, J. T. DeJong, and J. D. Bronner. 2019. "Progressive changes in liquefaction and cone penetration resistance across multiple shaking events in centrifuge tests." *J. Geotech. Geoen-viron. Eng.* 145 (3): 04018112. https://doi.org/10.1061/(ASCE)GT .1943-5606.0001995.
- Darendeli, M. B. 2001. "Development of a new family of normalized modulus reduction and material damping curves." Ph.D. dissertation, Dept. of Civil, Architectural, and Environmental Engineering, Univ. of Texas at Austin
- Derakhshandi, M., E. M. Rathje, K. Hazirbaba, and S. M. Mirhosseini. 2008. "The effect of plastic fines on the pore pressure generation characteristics of saturated sands." J. Soil Dyn. Eng. 28 (5): 376–386. https://doi.org/10.1016/j.soildyn.2007.07.002.
- Dobry, R., and T. Abdoun. 2015. "Cyclic shear strain needed for liquefaction triggering and assessment of overburden pressure factor K_{σ} ." *J. Geotech. Geoenviron. Eng.* 141 (11): 04015047. https://doi.org/10.1061/(ASCE)GT.1943-5606.0001342.
- Dobry, R., and T. Abdoun. 2017. "Recent findings on liquefaction triggering in clean and silty sands during earthquakes." J. Geotech. Geoenviron. Eng. 143 (10): 04017077. https://doi.org/10.1061/(ASCE)GT.1943-5606.0001778.
- Dobry, R., R. S. Ladd, F. Y. Yokel, R. M. Chung, and D. Powell. 1982.
 Prediction of pore water pressure buildup and liquefaction of sands during earthquakes by the cyclic strain method. Gaithersburg, MD: National Bureau of Standards.
- Dobry, R., K. H. Stokoe, R. S. Ladd, and T. L. Youd. 1981. "Liquefaction susceptibility from S-wave velocity." In Proc., ASCE National Convention, In Situ Tests to Evaluate Liquefaction Susceptibility. Reston, VA: ASCE.
- Donaldson, A. M. 2019. "Characterization of the small-strain stiffness of soils at an *in-situ* liquefaction test site." M.S. thesis, School of Civil and Construction Engineering, Oregon State Univ.
- Dowding, C. H., and R. D. Hryciw. 1986. "A laboratory study of blast densification of saturated sand." *J. Geotech. Eng.* 112 (2): 187–199. https://doi.org/10.1061/(ASCE)0733-9410(1986)112:2(187).
- Dyvik, R., T. Berre, S. Lacasse, and B. Raadim. 1987. "Comparison of truly undrained and constant volume direct simple shear tests." *Géotechnique* 37 (1): 3–10. https://doi.org/10.1680/geot.1987.37.1.3.
- El-Sekelly, W., T. Abdoun, and R. Dobry. 2016a. "Liquefaction resistance of a silty sand deposit subjected to preshaking followed by extensive liquefaction." *J. Geotech. Geoenviron. Eng.* 142 (4): 04015101. https:// doi.org/10.1061/(ASCE)GT.1943-5606.0001444.
- El-Sekelly, W., R. Dobry, T. Abdoun, and J. H. Steidl. 2016b. "Centrifuge modeling of the effect of preshaking on the liquefaction resistance of silty sand deposits." *J. Geotech. Geoenviron. Eng.* 142 (6): 04016012. https://doi.org/10.1061/(ASCE)GT.1943-5606.0001430.
- Esposito, M. P., R. D. Andrus, and W. M. Camp. 2014. "Ground freezing and sampling of Pleistocene sand near Charleston, South Carolina." *J. Geotech. Geoenviron. Eng.* 140 (1): 185–193. https://doi.org/10 .1061/(ASCE)GT.1943-5606.0000991.
- Evarts, R. C., J. O'Connor, and M. C. Charles. 2016. *Geologic map of the Sauvie Island quadrangle, Multnomah and Columbia Counties, Oregon, and Clark County, Washington*. Washington, DC: USGS.
- Fragaszy, R. J., and M. E. Voss. 1986. "Undrained compression behavior of sand." *J. Geotech. Eng.* 112 (3): 334–347. https://doi.org/10.1061/(ASCE)0733-9410(1986)112:3(334).
- Gallant, A. P., and R. J. Finno. 2016. "Stress redistribution after blast densification." J. Geotech. Geoenviron. Eng. 142 (11): 04016064. https://doi.org/10.1061/(ASCE)GT.1943-5606.0001497.
- Gao, Q., W. Lu, Z. Yang, P. Yan, and M. Chen. 2019. "Analysis of evolution of seismic components induced by a vertical blasthole." *Rock Mech. Rock Eng.* 52 (6): 1959–1977. https://doi.org/10.1007/s00603-018 -1680-1.
- Gianella, T. N., and A. W. Stuedlein. 2017. "Performance of driven displacement pile-improved ground in controlled blasting field tests." J. Geotech. Geoenviron. Eng. 143 (9): 04017047. https://doi.org/10 .1061/(ASCE)GT.1943-5606.0001731.
- Gohl, W. B., J. A. Howie, and C. E. Rea. 2001 "Use of controlled detonation of explosives for liquefaction testing." In *Proc.*, 4th Int. Conf. on

- Recent Advances in Geotechnical Earthquake Engineering and Soil Dynamics. Rolla, MO: Univ. of Missouri–Rolla.
- Gohl, W. B., M. G. Jefferies, J. A. Howies, and D. Diggle. 2000. "Explosive compaction: Design, implementation and effectiveness." *Géotechnique* 50 (6): 657–665. https://doi.org/10.1680/geot.2000.50.6.657.
- Handy, R. L. 1985. "The arch in soil arching." *J. Geotech. Eng.* 111 (3): 302–318. https://doi.org/10.1061/(ASCE)0733-9410(1985)111:3(302).
- Hazirbaba, K., and E. M. Rathje. 2009. "Pore pressure generation of silty sands due to induced cyclic shear strains." J. Geotech. Geoenviron. Eng. 135 (12): 1892–1905. https://doi.org/10.1061/(ASCE)GT.1943-5606 .0000147.
- Heelan, P. A. 1953. "Radiation from a cylindrical source of finite length." Geophysics 18 (3): 685. https://doi.org/10.1190/1.1437923.
- Heidari, T., and R. D. Andrus. 2012. "Liquefaction potential assessment of Pleistocene beach sands near Charleston, South Carolina." J. Geotech. Geoenviron. Eng. 138 (10): 1196–1208. https://doi.org/10.1061 /(ASCE)GT.1943-5606.0000686.
- Hryciw, R. D. 1986. "A study of the physical and chemical aspects of blast densification of sand." Ph.D. thesis, Dept. of Civil and Environmental Engineering, Northwestern Univ.
- Hsu, C. C., and M. Vucetic. 2004. "Volumetric threshold shear strain for cyclic settlement." J. Geotech. Geoenviron. Eng. 130 (1): 50–70. https://doi.org/10.1061/(ASCE)1090-0241(2004)130:1(58).
- Ishihara, K. 1968. "Propagation of compressional waves in a saturated soil." In *Proc., Int. Symp. Wave Propagation and Dynamic Properties* of Earth Materials, 195–206. Albuquerque, NM: University of New Mexico Press.
- Ishimwe, E., R. A. Coffman, and K. M. Rollins. 2018. "Analysis of post-liquefaction axial capacities of driven pile and drilled shaft foundations." In *Proc.*, *IFCEE* 2018, 272–283. Reston, VA: ASCE.
- Jana, A., A. M. Donaldson, A. W. Stuedlein, and T. M. Evans. 2021. "Deep, in-situ nonlinear dynamic testing of soil with controlled blasting: Instrumentation, calibration, and example application to a plastic silt deposit." Geotech. Test. J. 44 (5): GTJ20190426.
- Jana, A., and A. W. Stuedlein. 2020. "Monotonic, cyclic, and post-cyclic responses of an alluvial plastic silt deposit." *J. Geotech. Geoenviron. Eng.* 147 (3): 04020174. https://doi.org/10.1061/(ASCE)1090-0241 (2001)127:4(297).
- Kayen, R., R. E. S. Moss, E. M. Thompson, R. B. Seed, K. O. Cetin, A. Der Kiureghian, Y. Tanaka, and K. Tokimatsu. 2013. "Shear-wave velocity– based probabilistic and deterministic assessment of seismic soil liquefaction potential." *J. Geotech. Geoenviron. Eng.* 139 (3): 407–419. https://doi.org/10.1061/(ASCE)GT.1943-5606.0000743.
- Kevan, L. I., K. M. Rollins, R. A. Coffman, and E. Ishimwe. 2019. "Full-scale blast liquefaction testing in Arkansas USA to evaluate pile downdrag and neutral plane concepts." In *Proc.*, 7th Int. Conf. Earthquake Geotechnical Engineering, 12. Boca Raton, FL: CRC Press.
- Koester, J. P. 1994. "The influence of fines type and content on cyclic strength." In *Ground failures under seismic conditions*, 17–33. Reston, VA: ASCE.
- Kramer, S. L., and M. W. Greenfield. 2019. "The use of numerical analysis in the interpretation of liquefaction case histories." In *Proc. 7th Int. Conf. Earthquake Geotechnical Engineering*, 173–188. Boca Raton, FL: CRC Press.
- Ladd, R. S. 1977. "Specimen preparation and cyclic stability of sands." J. Geotech. Eng. Div. 103 (6): 535–547.
- Mahvelati, S., J. T. Coe, A. W. Stuedlein, P. Asabere, T. N. Gianella, and A. Kordjazi. 2020. "Recovery of small-strain stiffness following blast-induced liquefaction based on shear wave velocity measurements." Can. Geotech. J. https://doi.org/10.1139/cgj-2019-0658.
- Martin, G. R., W. D. L. Finn, and H. B. Seed. 1975. "Fundamentals of liquefaction under cyclic loading." *J. Geotech. Eng. Div.* 101 (5): 423–438.
- Mayne, P. W. 2007. Cone penetration testing: A synthesis of highway practice. NCHRP Rep. No. 368. Washington, DC: Transportation Research Board.
- Menq, F. Y. 2003. "Dynamic properties of sandy and gravelly soils." Ph.D. dissertation, Dept. of Civil, Architectural, and Environmental Engineering, Univ. of Texas.

- Mikkelsen, P. E., and G. E. Green. 2003. *Piezometers in fully grouted bore-holes*, 545–553. Oslo, Norway: Field Measurements in Geomechanics.
- Mitchell, J., and Z. Solymar. 1984. "Time-dependent strength gain in freshly deposited or densified sand." *J. Geotech. Eng.* 110 (11): 1559–1576. https://doi.org/10.1061/(ASCE)0733-9410(1984)110:11 (1559).
- Moss, R. E. S., R. B. Seed, R. E. Kayen, J. P. Stewart, A. Der Kiureghian, and K. O. Cetin. 2006. "CPT-based probabilistic and deterministic assessment of in situ seismic soil liquefaction potential." *J. Geotech. Geoenviron. Eng.* 132 (8): 1032–1051. https://doi.org/10.1061/(ASCE) 1090-0241(2006)132:8(1032).
- Mulilis, J. P., K. Arulanandan, J. K. Mitchell, C. K. Chan, and H. B. Seed. 1977. "Effects of sample preparation on sand liquefaction." *J. Geotech. Eng. Div.* 103 (2): 91–108. https://doi.org/10.1061/AJGEB6.0000387.
- Narin Van Court, W. A., and J. K. Mitchell. 1994. "Soil improvement by blasting." *J. Explos. Eng.* 12 (3): 34–41.
- Ni, M., T. Abdoun, R. Dobry, and W. El-Sekelly. 2021. "Effect of field drainage on seismic pore pressure buildup and K_{σ} under high overburden pressure." *J. Geotech. Geoenviron. Eng.* https://doi.org/10.1061/(ASCE)GT.1943-5606.0002536.
- Ni, M., T. Abdoun, R. Dobry, K. Zehtab, A. Marr, and W. El-Sekelly. 2020. "Pore pressure and K_{σ} evaluation at high overburden pressure under field drainage conditions. I: Centrifuge experiments." *J. Geotech. Geoenviron. Eng.* 146 (9): 04020088. https://doi.org/10.1061/(ASCE)GT .1943-5606.0002303.
- Park, S. S., and Y. S. Kim. 2013. "Liquefaction resistance of sands containing plastic fines with different plasticity." *J. Geotech. Geoenviron. Eng.* 139 (5): 825–830. https://doi.org/10.1061/(ASCE)GT.1943-5606.0000806.
- Park, T., and M. L. Silver. 1975. Dynamic soil properties required to predict the dynamic behavior of elevated transportation structures. Washington, DC: USDOT.
- Perry, J. I., C. H. Braithwaite, N. E. Taylor, and A. P. Jardine. 2015. "Behavior of moist and saturated sand during shock and release." *Appl. Phys. Lett.* 107 (17): 174102. https://doi.org/10.1063/1.4934689.
- Rathje, E., R. Phillips, W. J. Chang, and K. H. Stokoe. 2001. "Evaluating nonlinear response in situ." In *Proc., 4th Int. Conf. on Recent Advances in Geotechnical Earthquake Engineering and Soil Dynamics*. San Diego: Missouri S&T Library and Learning Resources.
- Rathje, E. M., W. J. Chang, and K. H. Stokoe. 2005. "Development of an in situ dynamic liquefaction test." *Geotech. Test. J.* 28 (1): 50–60.
- Roberts, J. N., K. H. Stokoe, B. R. Cox, and F. M. Menq. 2017. "Field and laboratory investigations into the behaviors of silty sands that leads to liquefaction triggering." In *Proc.*, 16th World Conf. on Earthquake. Santiago, Chile: Chilean Association of Seismology and Earthquake Engineering.
- Roberts, J. N., K. H. Stokoe, S. Hwang, B. R. Cox, Y. Wang, F. M. Menq, and S. van Ballegooy. 2016. "Field measurements of the variability in shear strain and pore pressure generation in Christchurch soils." In *Proc.*, 5th Int. Conf. on Geotechnical and Geophysical Site Characterisation. Sydney, NSW, Australia: Australian Geomechanics Society.
- Robertson, P. 2009. "Interpretation of cone penetration tests—A unified approach." *Can. Geotech. J.* 46 (11): 1337–1355. https://doi.org/10.1139/T09-065.
- Rollins, K. M., J. Anderson, A. McCain, and R. Goughnour. 2004. "Vertical composite drains for mitigating liquefaction hazard." In *Proc.*, 13th Int. Offshore and Polar Eng. Conf., 498–505. Shanghai, China: International Society of Offshore and Polar Engineers.
- Rollins, K. M., T. M. Gerber, J. D. Lane, and S. A. Ashford. 2005. "Lateral resistance of a full-scale pile group in liquefied sand." *J. Geotech. Geoenviron. Eng.* 131 (1): 115–125. https://doi.org/10.1061/(ASCE)1090-0241(2005)131:1(115).
- Rollins, K. M., L. J. Hales, S. A. Ashford, and W. M. Camp. 2006. "P-y curves for large diameter shafts in liquefied sand from blast

- liquefaction tests." In Seismic performance and simulation of pile foundations, 11–23. Reston, VA: ASCE.
- Rollins, K. M., and S. R. Strand. 2006. "Downdrag forces due to liquefaction surrounding a pile." In *Proc.*, 8th National Conf. on Earthquake Engineering, 10. Oakland, CA: Earthquake Engineering Research Institute.
- Sahadewa, A., D. Zekkos, R. D. Woods, and K. H. Stokoe. 2015. "Field testing method for evaluating the small-strain shear modulus and shear modulus nonlinearity of solid waste." *Geotech. Test. J.* 38 (4): 20140016. https://doi.org/10.1520/GTJ20140016.
- Sanchez-Salinero, I., J. M. Roesset, and K. H. Stokoe. 1986. Analytical studies of wave propagation and attenuation. Washington, DC: Air Force Office of Scientific Research.
- Schneider, J. A., and R. E. S. Moss. 2011. "Linking cyclic stress and cyclic strain based methods for assessment of cyclic liquefaction triggering in sands." *Géotech. Lett.* 1 (2): 31–36. https://doi.org/10.1680/geolett.11 .00021.
- Seed, H. B. 1979. "Soil liquefaction and cyclic mobility evaluation for level ground during earthquakes." *J. Geotech. Eng. Div.* 105 (2): 201–255. https://doi.org/10.1061/AJGEB6.0000768.
- Seed, H. B., I. M. Idriss, and I. Arango. 1983. "Evaluation of liquefaction potential using field performance data." J. Geotech. Eng. 109 (3): 458–482. https://doi.org/10.1061/(ASCE)0733-9410(1983)109:3(458).
- Stokoe, K. H., E. M. Rathje, and P. J. Axtell. 2005. "Development of an in situ method to measure the nonlinear shear modulus of soil." In *Proc.*, *Int. Conf. on Soil Mechanics and Geotechnical Engineering*, 751. Rotterdam, Netherlands: A.A. Balkema.
- Stokoe, K. H., J. N. Roberts, S. Hwang, B. Cox, F. M. Menq, and S. Van Ballegooy. 2014. "Effectiveness of inhibiting liquefaction triggering by shallow ground improvement methods: Initial field shaking trials with T-Rex at one site in Christchurch New Zealand." In Proc., New Zealand—Japan Workshop on Soil Liquefaction during Recent Large-Scale Earthquakes, 193–202. Boca Raton, FL: CRC Press.
- van Ballegooy, S., J. N. Roberts, K. H. Stokoe, B. R. Cox, F. J. Wentz, and S. Hwang. 2015. "Large-scale testing of shallow ground improvements using controlled staged-loading with T-Rex." In *Proc.*, 6th Int. Conf. on Earthquake Geotechnical Engineering. Boca Raton, FL: CRC Press.
- Vanbrabant, F., E. P. Chacón, and L. A. Quiñones. 2002. "P and S Mach waves generated by the detonation of a cylindrical explosive charge experiments and simulations." *Fragblast* 6 (1): 21–35. https://doi.org/10.1076/frag.6.1.21.8849.
- Weaver, T. J., S. A. Ashford, and K. M. Rollins. 2005. "Response of 0.6 m cast-in-steel-shell pile in liquefied soil under lateral loading." J. Geotech. Geoenviron. Eng. 131 (1): 94–102. https://doi.org/10.1061/(ASCE)1090-0241(2005)131:1(94).
- Xiao, Y., L. Long, T. M. Evans, H. Zhou, H. Liu, and A. W. Stuedlein. 2018. "Effect of particle shape on stress-dilatancy responses of medium-dense sands." *J. Geotech. Geoenviron. Eng.* 145 (2): 04018105. https://doi.org/10.1061/(ASCE)GT.1943-5606.0001994.
- Youd, T. L., and I. M. Idriss. 2001. "Liquefaction resistance of soils: Summary report from the 1996 NCEER and the 1998 NCEER/NSF workshops on the evaluation of liquefaction resistance of soils." *J. Geotech. Geoenviron. Eng.* 127 (4): 297–313. https://doi.org/10.1061/(ASCE)1090-0241(2001)127:4(297).
- Zeghal, M., and A. W. Elgamal. 1994. ""Analysis of site liquefaction using earthquake records." *J. Geotech. Eng.* 120 (6): 996–1017. https://doi.org/10.1061/(ASCE)0733-9410(1994)120:6(996).
- Zhang, B., K. H. Stokoe, and F. M. Menq. 2019. "Field measurement of linear and nonlinear shear moduli during large-strain shaking." In Earthquake geotechnical engineering for protection and development of environment and constructions. Rome, Italy: Associazione Geotecnica Italiana.

SUPPLEMENTAL MATERIALS

ASCE Journal of Geotechnical and Geoenvironmental Engineering

Dynamic In Situ Nonlinear Inelastic Response of a Deep Medium-Dense Sand Deposit

Amalesh Jana and Armin W. Stuedlein

DOI: 10.1061/(ASCE)GT.1943-5606.0002523

© ASCE 2021

www.ascelibrary.org

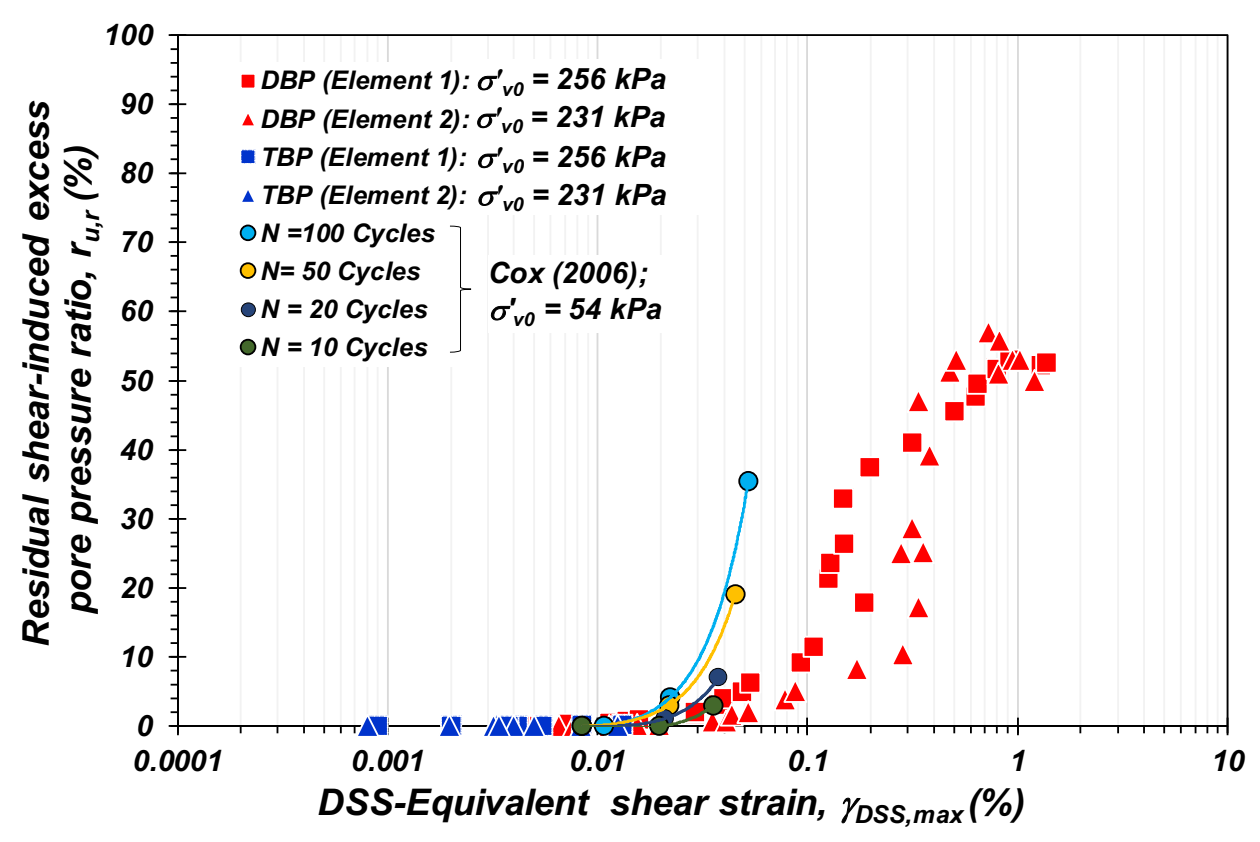


Figure S1. Comparison of the variation of the residual shear-induced excess pore pressure ratio with maximum DSS-equivalent shear strain of the medium dense sand deposit (Sand Array) from the Test and Deep Blast Programs under high vertical effective stresses to the response of sand under medium vertical effective stresses reported by Cox (2006).

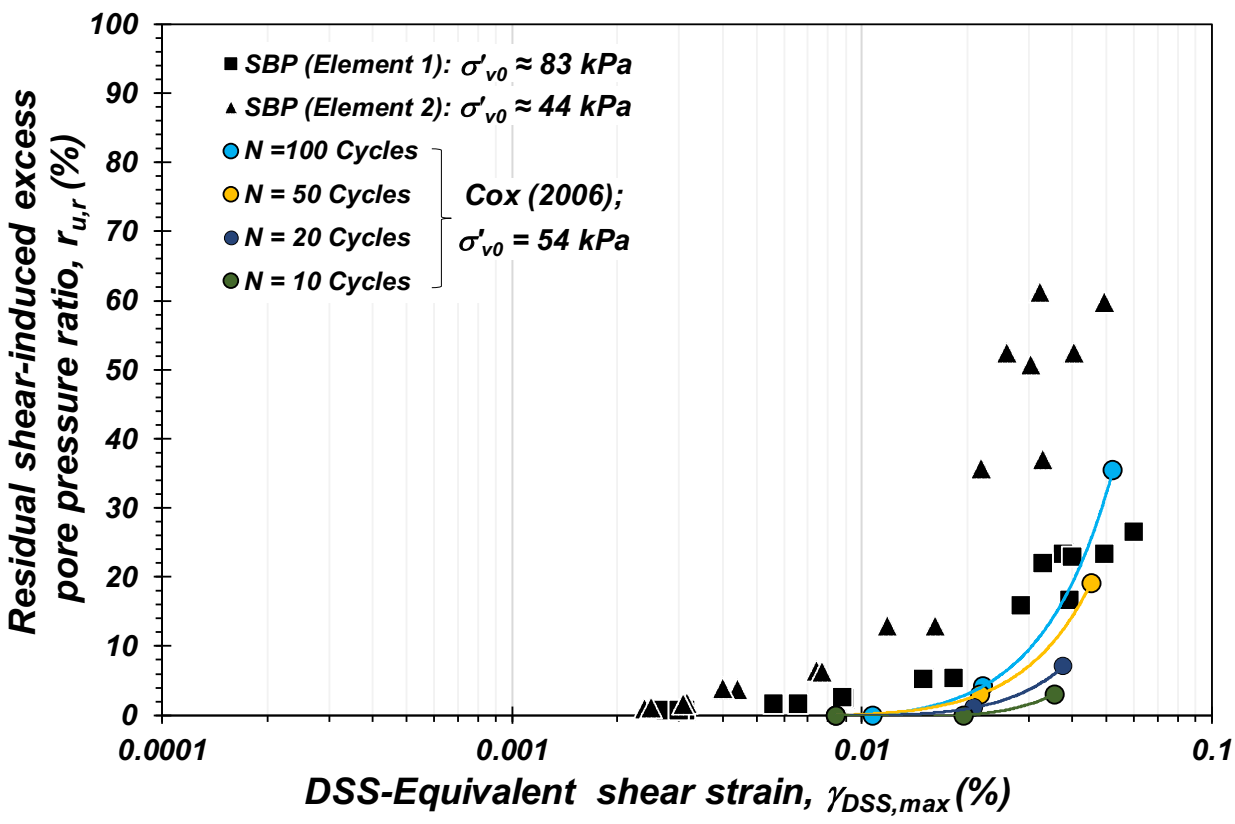


Figure S2. Comparison of the variation of the residual shear-induced excess pore pressure ratio with maximum DSS-equivalent shear strain of the medium dense sand deposit (Sand Array) from the Shallow Blast Programs under medium vertical effective stresses to the response of sand under medium vertical effective stresses reported by Cox (2006).

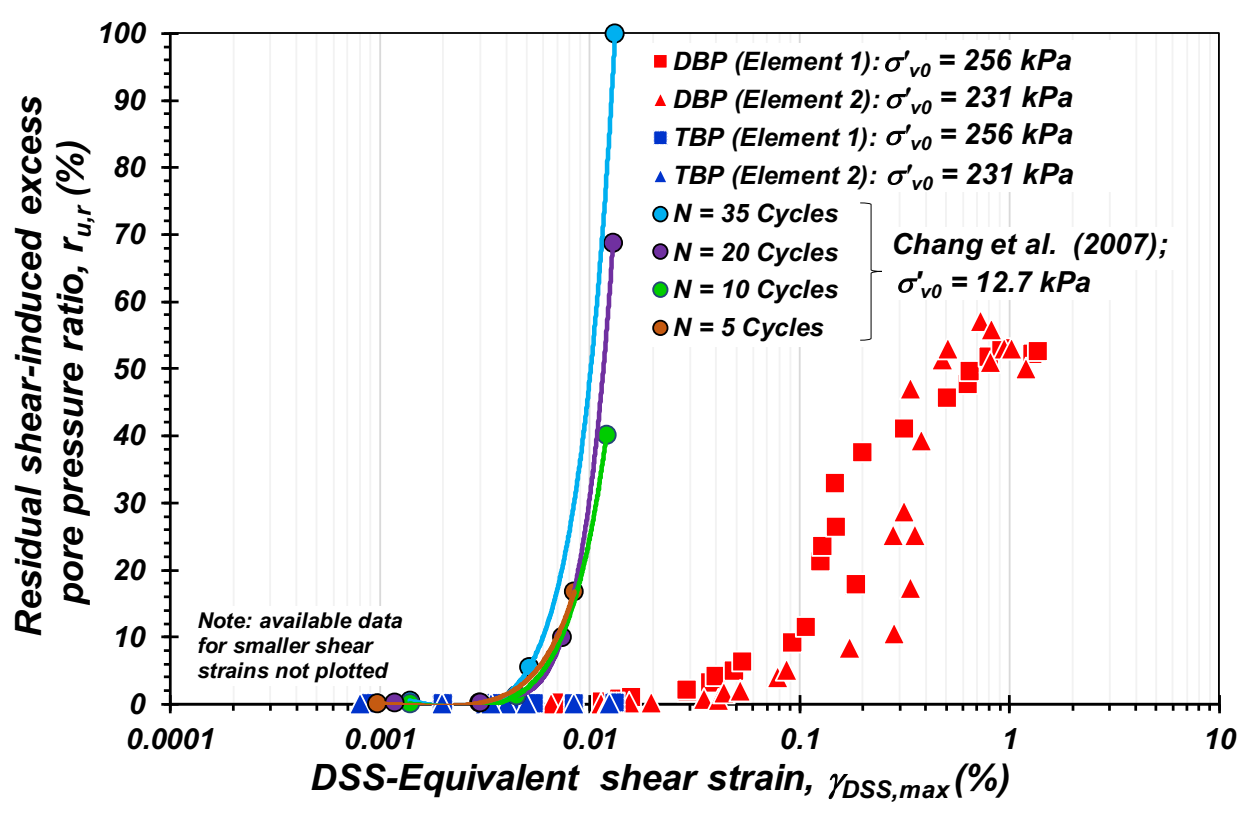


Figure S3. Comparison of the variation of the residual shear-induced excess pore pressure ratio with maximum DSS-equivalent shear strain of the medium dense sand deposit (Sand Array) from the Test and Deep Blast Programs under high vertical effective stresses to the response of sand under low vertical effective stresses reported by Chang et al. (2007).

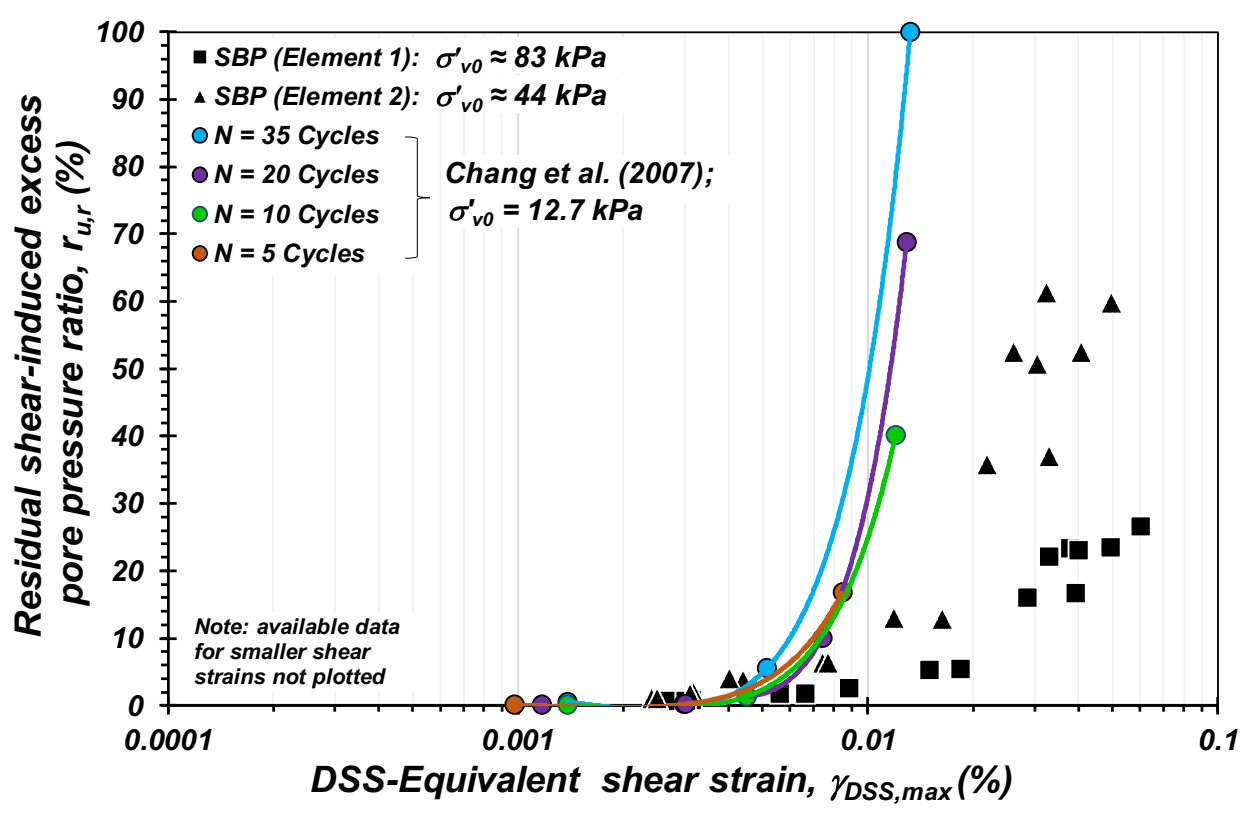


Figure S4. Comparison of the variation of the residual shear-induced excess pore pressure ratio with maximum DSS-equivalent shear strain of the medium dense sand deposit (Sand Array) from the Shallow Blast Programs under medium vertical effective stresses to the response of sand under low vertical effective stresses reported by Chang et al. (2007).

References

- Chang, W. J., E. M. Rathje, K. H. Stokoe II, and K. Hazirbaba. 2007. "In Situ Pore Pressure Generation Behavior of Liquefiable Sand." *J. Geotech. Geoenviron. Eng.* 133: 921–931.
- Cox, B.R. 2006. "Development of a direct test method for dynamically assessing the liquefaction resistance of soils in situ." *PhD dissertations*, University of Texas at Austin, 498 pp.